IDENTIFICATION OF SPATIAL VARIABILITY IN BRIDGE FOUNDATION INPUT MOTIONS: THEORETICAL BASIS

E. Taciroglu and S.F. Ghahari

Department of Civil & Environmental Engineering
University of California, Los Angeles

Abstract

This paper presents progress made towards the identification of spatial variability in bridge Foundation Input Motions (FIMs) in a project funded by the California Geological Survey. The term spatial variability denotes here the differences in amplitude and phase of seismic motions recorded over extended areas, and it is well accepted that lifeline structures, such as long bridges, are prone to its effects, because they extend over relatively long distances. The specific objective of the project is to identify FIMs from response signals recorded by instrumented bridges during the South Napa 2014 earthquake, decompose them to bedrock motions and site effects, and finally quantify the spatial variability for each bridge structure. In this progress paper, we present initial observations, data selection, and the theoretical basis of the methodology that will be employed to process the recorded data. The overall methodology comprises two novel approaches (*i*) for output-only identification of bridges under multiple support excitations, and (*ii*) for blind identification of bedrock motions and site effects from two (or more) ground-surface motions (FIMs). The said two methods are briefly described and numerically verified in the present paper. The first method will be employed to extract FIMs from spatially sparse measurements of bridge responses, while the second one will be used to further identify the site effects and bedrock motions from the recovered FIMs.

Introduction

Today, highly detailed and accurate Finite Element (FE) models of bridges are created routinely, using broadly available commercial software. However, accurate seismic response predictions for bridges are still constrained by our ability to apply physically accurate/consistent input motions. Long-span bridges are known to be prone to the so-called "*spatially variability*" effects, which is a term used for collectively denoting the differences in amplitude and phase of seismic motions recorded over extended areas (Zerva & Zervas, 2002), due to their longitudinal extents (Zerva, et al., 1988; Hao, et al., 1989; Nazmy & Abdel-Ghaffar, 1992; Lupoi, et al., 2005; Burdette, et al., 2008).

In current practice, California Department of Transportation (Caltrans), for example, takes spatial variability into account by synthetically producing ground motions at each pier of the bridge using one-dimensional site-response analyses. That is, the seismic motion estimated on the bedrock—which is typically a "de-convoluted" version of the Free-Field Motion (FFM)—is transferred to the surface at each pier using specific soil properties at each pier's site. In the presence of kinematic soil-structure interaction effects[1], these Free-Field Motions (FFMs) must

[1] Kinematic interaction is caused by the stiffness contrast of the foundation system from its surrounding soil media.

also be converted to the so-called Foundation Input Motions (FIMs) (see **Figure 1**). Therefore, while ground motions at the bedrock of the bridge site may be uniform, a long bridge may still experience differing excitations at different piers. While, several other factors—such as local soil nonlinearity and path effects—may be involved in spatial variability, the approach currently used by Caltrans only attempts to take the *site effects* into account. Even in this particular issue, the procedure employed has numerous shortcomings. To wit, the procedure assumes vertically propagating horizontally polarized waves, which is not necessarily true. Also, the deconvolution procedure may introduce numerical errors (including unrealistically large motions at the bedrock). Furthermore, conversion of FFMs into FIMs may introduce significant errors—especially when local nonlinearities and other spatial variability effects are present—, and at the present time, there is no validated procedure to carry out this task.

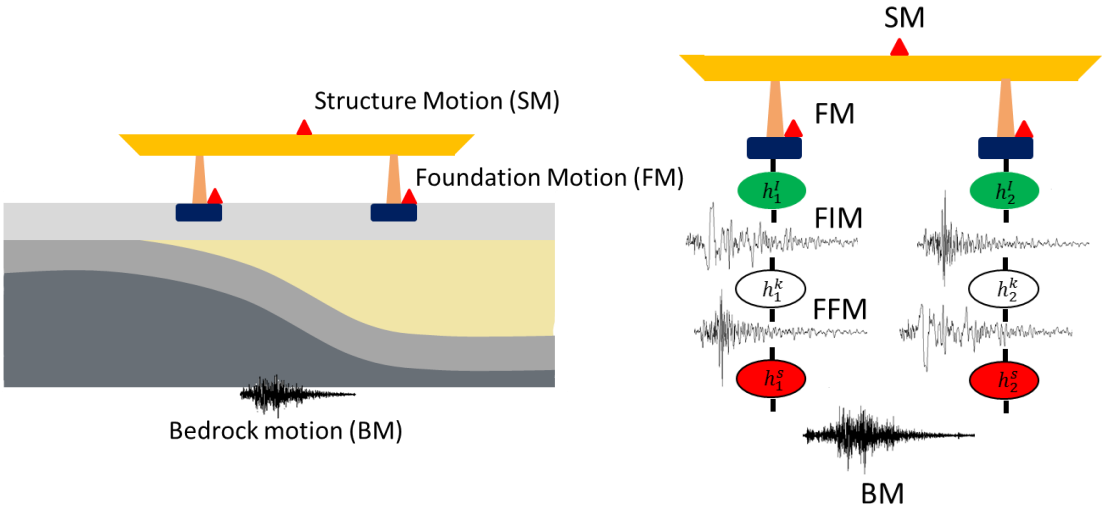

Figure 1. Current approach to bridge analysis under multiple support excitations.

Given these difficulties, the back-calculation of FIMs from real-life data is a key capability to study spatial variability effects and to validate (or to refute) new or existing procedures that predict the foundation input motions. Under the general umbrella of seismic monitoring, a specific motivation for instrumenting long-span bridges in California was indeed to provide a quantitative basis for evaluating how these structures respond to spatially varying ground motions (Kurata, et al., 2012). Simple comparisons of pier to pier motions recorded at the foundation level will not illuminate the subject matter, as these records are polluted by kinematic and inertial interaction effects, and therefore, will only provide a limited understanding/quantification of spatial variability of seismic input motions for bridges. In the current project—the first-half progress of which is presented in this paper—a novel approach is devised to:

(1) back-calculate FIMs from sparsely measured acceleration signals recorded during the 2014 South Napa earthquake at several CSMIP-instrumented bridges;

(2) back-calculate bedrock motions and site effects at each pier (under specific conditions).

To carry out the first step, we adopt a time-domain output-only identification method originally developed by Huang et al. (Huang, et al., 2010) for our problem. To achieve the

second goal, we devise a novel blind identification method (Ghahari, et al., 2016) through which the bedrock motions and site effects can be back-calculated using FIMs identified in the first step.

In what follows, we first present a review of available bridge data from the South Napa event, identify those recorded motions that exhibit evidence of the presence of spatial variability, and select the data sets suitable for the current study. We then provide the details of both of the identification methods mentioned above, as well as their verification through synthetic data sets.

Available Data

As mentioned above, this project will use data recorded during the 2014 South Napa earthquake. This M_w-6.0 earthquake occurred on August 24, 2014 near the well-known West Napa Fault. The epicenter was at 38.216N and 122.312W—i.e., approximately 9 km SSW of Napa, California and 82 km WSW of Sacramento, California. It was the most significant event in Northern California since the M6.9 Loma Prieta earthquake of 1989 (Shakal, et al., 2014).

17 of the 80+ instrumented bridges recorded the South Napa earthquake, which are listed in **Table 1**. The locations of these bridges and the earthquake's epicenter are displayed on **Figure 2**. The table also provides the approximate lengths of the 17 bridges, 11 of which are at least 1km-long. This means that they are ideal candidates for studying and quantifying the effects of spatially variability. Incidentally, the Peak Structural Accelerations (PSAs) recorded on most of these bridges during the 2014 South Napa earthquake are significant, which provides an opportunity to work with favorable Signal-To-Noise (SNR) ratios. Moreover, more than half of the 17 bridges have a nearby ground motion station that recorded Free-Field Motions (FFMs). Data from these stations will enable the calculation of Transfer Functions between the FFMs and FIMs.

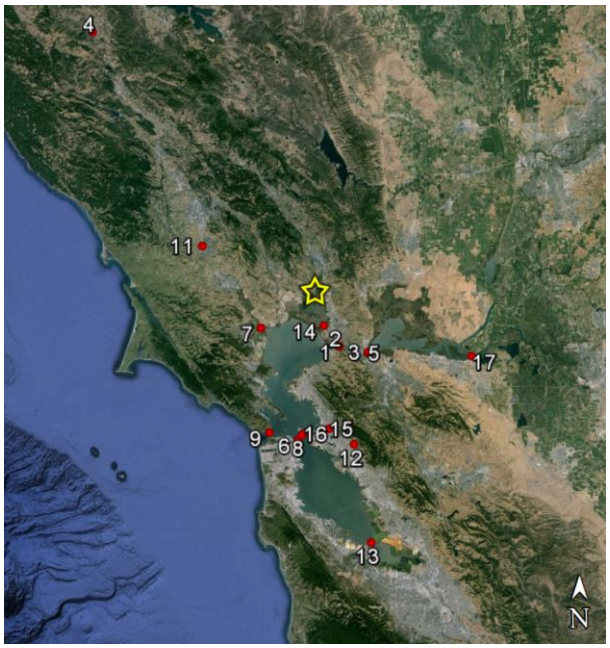

Figure 2. Geographic distribution of the 17 instrumented bridges around the epicenter of the 2014 South Napa Earthquake.

Table 1. List of all bridges that recorded the 2014 South Napa Earthquake.

No.	Name	Station No.	Length (m)	Epic. Dist. (km)	Fault Dist. (km)	PGA (*g*)	PSA (*g*)
1	Vallejo - Carquinez/I80 East Bridge	68184	1021	18.9	19.4	0.149	1.085
2	Vallejo - Carquinez/I80 West Bridge	68185	1056	18.9	19.3	0.085	0.790
3	Benicia - Martinez/I680 East Bridge	68322	2265	25.5	25.7	0.063	0.122
4	Hopland - Hwy 101/Railroad Bridge	69760	94.5	107.0	98.2	0.062	0.017
5	Benicia - Martinez/I680 West Bridge	68682	1894	25.7	25.9	0.031	0.343
6	San Francisco - Bay Bridge/West	58632	3137	46.6	47.2	0.031	0.146
7	Novato -Hwy37 /Petaluma River Bridge	68778	665	19.7	20.6	0.024	0.062
8	Oakland - SF Bay Bridge/East: YBITS	58602	NA	44.8	45.5	0.024	0.047
9	San Francisco - Golden Gate Bridge	58700	2789	46.1	46.8	0.012	0.181
10	Oakland - SF Bay Bridge/East: Skyway	58601	2085	43.9	44.5	0.002	0.054
11	Rohnert Park - Hwy 101 Bridge	68717	86	37.6	33.6	NA	0.119
12	Oakland - Hwy 580/13 Interchange Bridge	58656	86	49.4	49.9	NA	0.027
13	San Francisco Bay - Dumbarton Bridge	58596	2620	80.7	81.2	NA	0.055
14	Vallejo - Hwy 37/Napa River Bridge	68065	1000	11.1	11.6	NA	0.657
15	Oakland - Hwy 580/24 Interchange Bridge	58657	1000	43.1	43.7	NA	0.092
16	Oakland - SF Bay Bridge/East: SAS	58600	NA	44.5	45.2	NA	0.162
17	Antioch - San Joaquin River Bridge	67771	2874	53.9	--	NA	0.092

Initial Observation

Since the FIMs are not directly available due to reasons mentioned earlier, and need to be back-calculated, we study here the spatial variability of input motions by using only the recorded signals on foundations and on the ground surface as a preliminary investigation. To this end, we calculate the cross-covariance among different locations for each bridge. We use the cross-correlation technique in the time-domain to quantify the similarity between two delayed accelerograms (Bendat & Piersol, 1980). This common signal processing technique is frequently used in a variety of engineering applications. The cross-covariance function is the correlation between series (acceleration records) shifted against one another as a function of delay or lag. The function exhibits distinct peaks at the lag value that corresponds to the precise time-delay between two otherwise similar accelerograms. The expression for the cross-covariance function for two discrete-time $s_i[n]$ and $s_j[n]$ accelerograms at lag k is calculated as

$$c_{ij}[k] = \frac{1}{N}\sum_{n=0}^{N-k}(s_i[n] - \bar{s}_i)\ (s_j[n+k] - \bar{s}_j) \qquad 1)$$

where $k = 0, 1, \cdots, N-1$, and N is number of time samples. Here, $\bar{s}_i$ and $\bar{s}_j$ indicate the mean values of the two signals. It is also possible to calculate $c_{ij}[k]$ for negative lags, which are easily obtained by changing the i and j sub-indices at the summation above. $c_{ij}[k]$ are usually normalized with the square-root of $c_{ii}[0]$ and $c_{jj}[0]$ to keep the value of covariance between −1 and +1. This normalized value is termed the *cross-correlation*. A cross-correlation equal to −1 or +1 denotes two signals that are identical except with a time lag, whereas a cross-correlation close to zero means that that they are not similar.

As an example, we present results of correlation analysis for one of the bridges listed in **Table 1** (similar results were observed for other bridges and are omitted here for the sake of brevity). **Figure 3** displays the instrumentation layout for CSMIP station No. 68184. The sensors that are marked with circles on this figure indicate those for which we calculated the cross-correlation values. Maximum values of cross-correlations are also shown in **Figure 3** for both longitudinal and transverse directions. As seen, except for those sensors that are very close to each other, the cross-correlation values are very small. This is more significant for the transverse direction. In the longitudinal direction—for example channels 5 and 47—, the higher values of cross-correlation are actually related to the system's response, but not the ground motions.

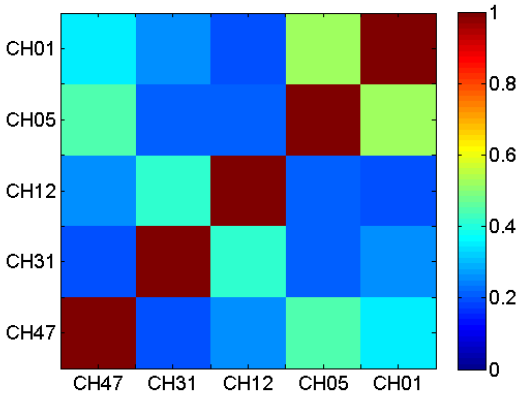

(a) Longitudinal direction

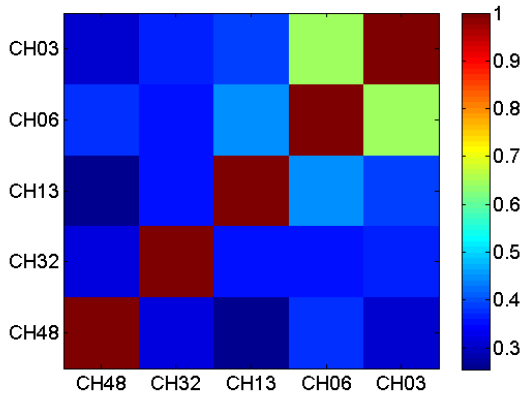

(b) Transverse direction

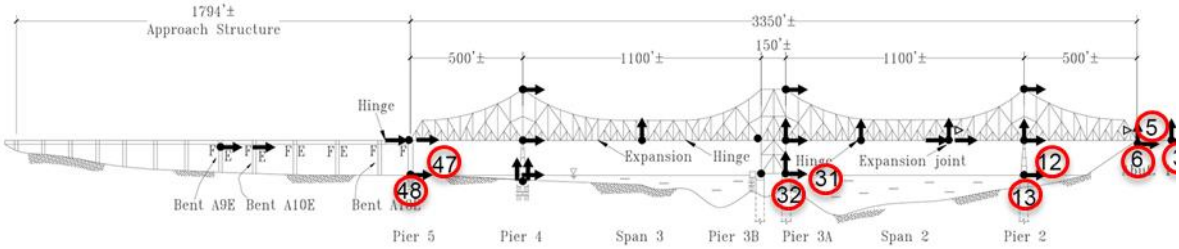

(c) Instrumentation layout

Figure 3. Spatial variability observed in CSMIP68184.

Data Selection

Not all of the 17 bridges introduced earlier are suitable for our study. No data are available for bridge No. 4 (CSMIP69760) in CESMD[2]. Two other bridges (CSMIP68717 and 58656) are very short, so they are not useful for studying spatial variability. Since having instruments on the foundation level is a crucial factor in the present study, bridge No. 7 (CSMIP68778) is also excluded as it does not have any sensor on its foundation level. The same limitation exits for bridges No. 14 and No. 15 (CSMIP68065 and 58657, respectively), and thus, they are also excluded. The level of vibration recorded on bridge No. 13 (CSMIP58596) is too small; the PSA is ~0.05g and is measured on channels 37 and 38 (i.e., two vertical channels at the edge of the main span). This indicates that the recorded motions are mostly free vibration, and thus, this bridge cannot be processed through the proposed identification method. As such, it is excluded as well. The level of vibration on two other bridges CSMIP58601 and 58602 is also very small. However, these two bridges—along with a third one (CSMIP58600)—create a system of connected bridges as shown in **Figure 4**. According to CESMD, a maximum structural acceleration of 0.162g is recorded on CSMIP58600, which makes the analysis of this bridge system a worthy attempt. However, no data appears available for the important channels (see **Figure 5** for instrumentation layout)[3]. As such, this bridge is also excluded.

Having excluded bridges mentioned above, there are then **7 bridges** left, whose data recorded during the 2014 South Napa earthquake can be analyzed to investigate spatial variability of FIMs. These 7 bridges are: CSMIP 68184, 68185, 68322, 68682, 58632, 58700, and 67771.

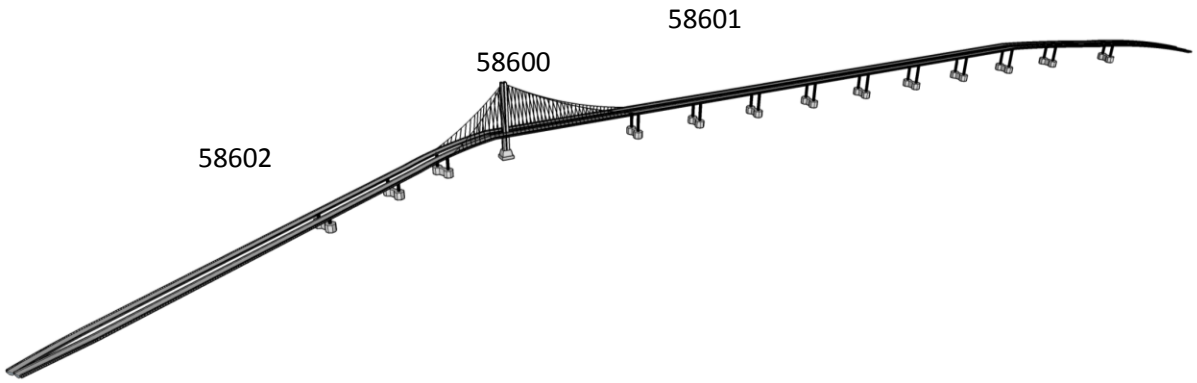

Figure 4. Eastern Oakland – San Francisco Bay Bridge.

[2] www.strong motioncenter.org

[3] For example, there is no data for channels 1 to 6 (foundation level of Pier W2), channels 25 to 30 (foundation level of Pier W2), and channels 68 to 73 (foundation level of Pier W2). Moreover, some channels on the deck—namely, channels 7 to 11, 12 to 15, 31 to 34 or 64 to 67—are missing data (last update 09/24/2016).

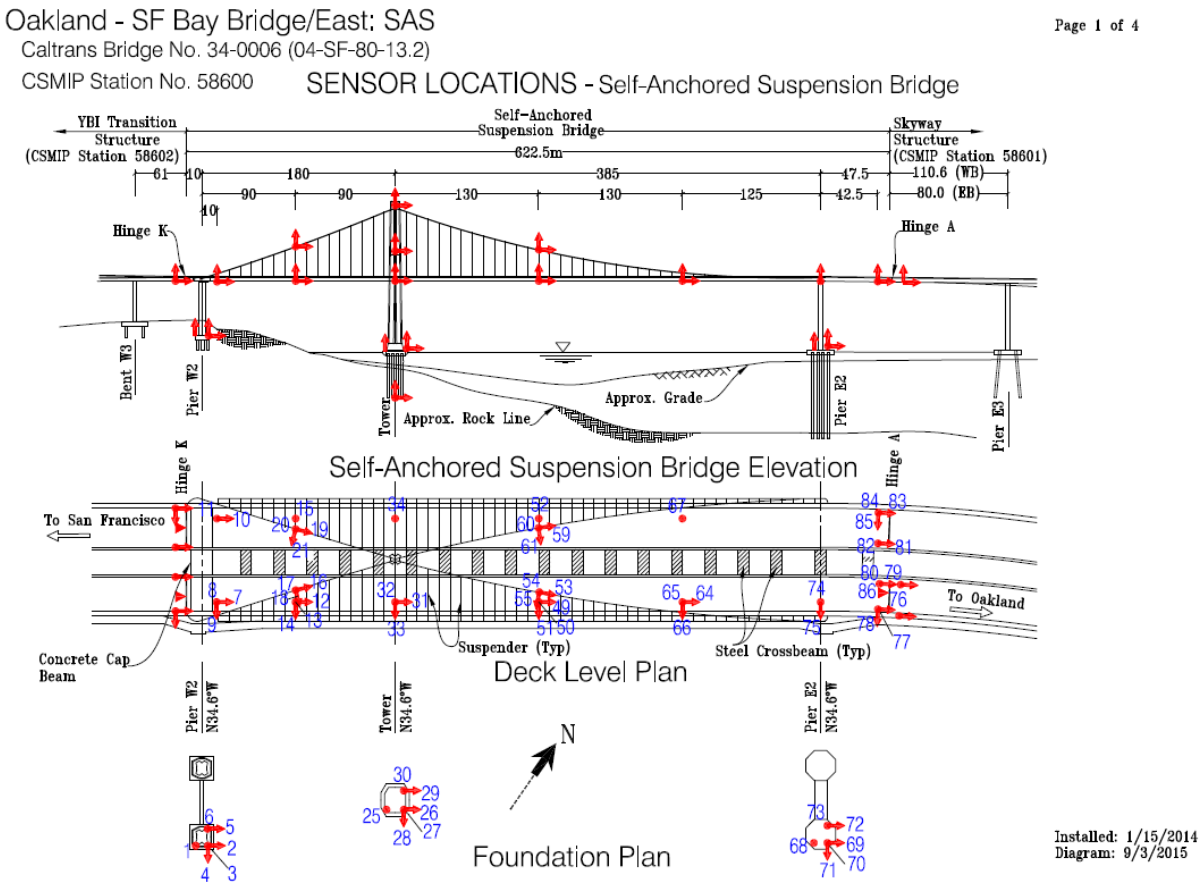

Figure 5. Instrumentation layout of CSMIP Station 58600.

Identification Methods

Part I: FIMs Estimation through Quadratic Sum-Squares Error

Dynamic Equation of Motion of Soil-Foundation-Structure System under Several FIMs

A schematic representation of the problem under study is shown in **Figure 6**. As seen, the bridge structure is subjected to several and different unknown Free-Field Motions (FFMs) at its piers. These FFMs are first converted to FIMs through unknown Kinematic Interaction (KI) filters and excited the bridge supported on flexible soil-foundation Impedance Functions (IFs). Herein, we assume that an initial (*uncertain*) Finite Element (FE) model of the bridge supported on *uncertain* IFs is available. Also, responses of the system at several locations on the bridge and foundation are measured as absolute accelerations through sensors. In what follows, a method is described, with which unknown FIMs, IFs, and unknown parameters of the *superstructure* are all identified simultaneously along with their uncertainties.

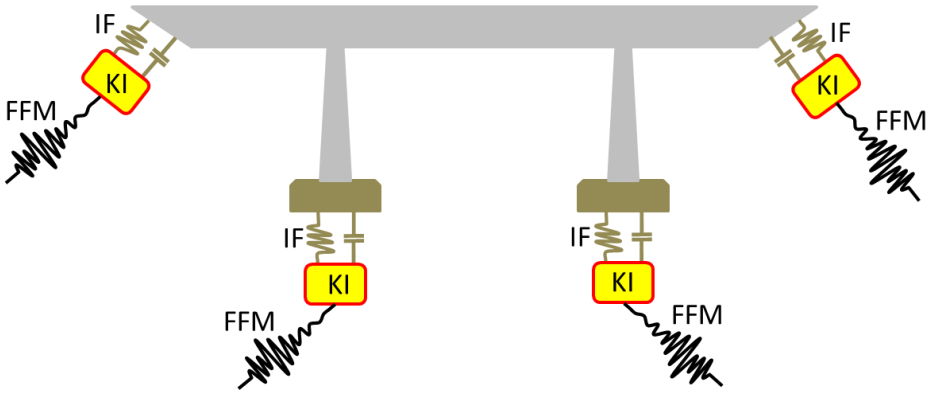

Figure 6. Lumped model of a multi-span bridge.

The equation of dynamic equilibrium for all the Degrees-Of-Freedom (DOFs) (n structure-foundation and n_g foundation-soil DOFs) is written in partitioned form as (Chopra, 2001)

$$\begin{bmatrix} \mathbf{M} & \mathbf{M}_g \\ \mathbf{M}_g{}^T & \mathbf{M}_{gg} \end{bmatrix} \begin{Bmatrix} \ddot{\boldsymbol{x}}(t) \\ \ddot{\boldsymbol{x}}_{\boldsymbol{g}}(t) \end{Bmatrix} + \begin{bmatrix} \mathbf{D} & \mathbf{D}_g \\ \mathbf{D}_g{}^T & \mathbf{D}_{gg} \end{bmatrix} \begin{Bmatrix} \dot{\boldsymbol{x}}(t) \\ \dot{\boldsymbol{x}}_{\boldsymbol{g}}(t) \end{Bmatrix} + \begin{bmatrix} \mathbf{K} & \mathbf{K}_g \\ \mathbf{K}_g{}^T & \mathbf{K}_{gg} \end{bmatrix} \begin{Bmatrix} \boldsymbol{x}(t) \\ \boldsymbol{x}_{\boldsymbol{g}}(t) \end{Bmatrix} = \begin{Bmatrix} \mathbf{0} \\ \boldsymbol{P}_g(t) \end{Bmatrix} \quad 2)$$

where **M**, **D**, and **K** are $n \times n$ mass, damping and stiffness matrices of the foundation-structure, respectively. Matrices $\mathbf{M}_g$, $\mathbf{D}_g$, and $\mathbf{K}_g$ are $n \times n_g$ mass, damping, and stiffness matrices of the foundation-soil interface, while $\mathbf{M}_{gg}$, $\mathbf{D}_{gg}$, and $\mathbf{K}_{gg}$ matrices are related to soil's DOFs. In Eq. (2), $\boldsymbol{x}(t)$ is a vector that contains the absolute displacement response of all n structure-foundation DOFs, while $\dot{\boldsymbol{x}}(t)$, and $\ddot{\boldsymbol{x}}(t)$ are their corresponding velocity and acceleration vectors. $\boldsymbol{x}_g(t) = [x_{g,1}(t) \quad \cdots \quad x_{g,n_g}(t)]^T$ and whose time derivatives $\dot{\boldsymbol{x}}_g(t)$ and $\ddot{\boldsymbol{x}}_g(t)$ are vectors containing prescribed the Foundation Input Motions (FIMs) as displacement, velocity, and acceleration at all n_g foundation-soil interface DOFs. As there is no external force on the structure-foundation DOFs, the only forces needed for applying FIMs is $\boldsymbol{P}_g(t)$, as shown in Eq. (2).

The absolute displacement of the bridge (structure-foundation) can be written as the superposition of displacement produced by the static application of the prescribed FIMs at each time instant $\boldsymbol{u}^s(t)$ and dynamic response with respect to the statically deformed position $\boldsymbol{u}(t)$ as

$$\begin{Bmatrix} \boldsymbol{x}(t) \\ \boldsymbol{x}_g(t) \end{Bmatrix} = \begin{Bmatrix} \boldsymbol{u}^s(t) \\ \boldsymbol{x}_g(t) \end{Bmatrix} + \begin{Bmatrix} \boldsymbol{u}(t) \\ \mathbf{0} \end{Bmatrix} \quad 3)$$

As $\boldsymbol{u}^s(t)$ is produced by static deformation of the bridge under static application of $\boldsymbol{x}_g(t)$, their relationships are governed by static equilibrium as follows

$$\begin{bmatrix} \mathbf{K} & \mathbf{K}_g \\ \mathbf{K}_g{}^T & \mathbf{K}_{gg} \end{bmatrix} \begin{Bmatrix} \boldsymbol{u}^s(t) \\ \boldsymbol{x}_g(t) \end{Bmatrix} = \begin{Bmatrix} \mathbf{0} \\ \boldsymbol{P}_g^s(t) \end{Bmatrix} \quad 4)$$

where $\boldsymbol{P}_g^s(t)$ is needed force at each time to impose $\boldsymbol{x}_g(t)$. It is trivial that $\boldsymbol{P}_g^s(t)$ would be zero if the system is statically determinate or all foundation-soil interface nodes move in compatible manner (e.g., identical horizontal FIMs).

The first partition of the Eq. (2) can be rewritten using mentioned above static and dynamic parts as

$$\mathbf{M}\,\ddot{\boldsymbol{u}}(t) + \mathbf{D}\,\dot{\boldsymbol{u}}(t) + \mathbf{K}\,\boldsymbol{u}(t) = -\left[\mathbf{M}\,\ddot{\boldsymbol{u}}^{s}(t) + \mathbf{M}_g\ddot{\boldsymbol{x}}_g(t)\right] - \left[\mathbf{D}\,\dot{\boldsymbol{u}}^{s}(t) + \mathbf{D}_g\dot{\boldsymbol{x}}_g(t)\right] \quad 5)$$

The term $\left[\mathbf{K}\,\boldsymbol{u}^{s}(t) + \mathbf{K}_g\boldsymbol{x}_g(t)\right]$ has been removed from right-hand-side of the equation above, because it is zero, based on the first partition of Eq. (4). In Eq. (5), it is more favorable to replace the quasi-static velocity and acceleration using their FIMs' counterparts, because $\mathbf{K}\,\boldsymbol{u}^{s}(t) + \mathbf{K}_g\boldsymbol{x}_g(t) = \mathbf{0}$. So, Eq. (5) can be rewritten as

$$\mathbf{M}\,\ddot{\boldsymbol{u}}(t) + \mathbf{D}\,\dot{\boldsymbol{u}}(t) + \mathbf{K}\,\boldsymbol{u}(t) = -\left[\mathbf{M}\,\mathbf{L} + \mathbf{M}_g\right]\ddot{\boldsymbol{x}}_g(t) - \left[\mathbf{D}\,\mathbf{L} + \mathbf{D}_g\right]\dot{\boldsymbol{x}}_g(t) \quad 6)$$

where $\mathbf{L} = -\mathbf{K}^{-1}\mathbf{K}_g$ is $n \times n_g$ influence matrix. Each column of the matrix $\mathbf{L}$, say $\boldsymbol{l}_l$, is a vector that assigns the influence of each input acceleration, $x_{g,l}(t)$, on the system's response; and is a function of internal and boundary stiffnesses. Damping term in Eq. (6) is usually small relative to the inertia term, and may be dropped (it is exactly zero when damping matrices are stiffness proportional). Moreover, for lumped mass systems, the mass matrix is diagonal and off the diagonal matrix $\mathbf{M}_g$ will be zero. So, Eq. (6) can be written in its final form as

$$\mathbf{M}\,\ddot{\boldsymbol{u}}(t) + \mathbf{D}\,\dot{\boldsymbol{u}}(t) + \mathbf{K}\,\boldsymbol{u}(t) = -\mathbf{M}\,\mathbf{L}\ddot{\boldsymbol{x}}_g(t) \quad 7)$$

Finally by replacing $\boldsymbol{u}(t)$ by $\boldsymbol{x}(t) - \boldsymbol{u}^{s}(t)$ in Eq. (7), equation of motion can be expressed in absolute framework as

$$\mathbf{M}\,\ddot{\boldsymbol{x}}(t) + \mathbf{D}\,\dot{\boldsymbol{x}}(t) + \mathbf{K}\,\boldsymbol{x}(t) = \mathbf{D}\,\mathbf{L}\,\dot{\boldsymbol{x}}_g(t) + \mathbf{K}\,\mathbf{L}\,\boldsymbol{x}_g(t) \quad 8)$$

The Identification Method

Eq. (8) can be written in the state-space as

$$\dot{\boldsymbol{z}}(t) = \mathbf{A}_c\,\boldsymbol{z}(t) + \mathbf{B}_c\,\boldsymbol{f}(t) + \boldsymbol{w}(t) \quad 9)$$

where $\boldsymbol{z}(t) = [\boldsymbol{x}(t)^T \quad \dot{\boldsymbol{x}}(t)^T]^T$ is $2n \times 1$ state vector, $\boldsymbol{f}(t) = \left[\boldsymbol{x}_g(t)^T \quad \dot{\boldsymbol{x}}_g(t)^T\right]^T$ is $2n_g \times 1$ excitation vector and continuous-time transition and input matrices $\mathbf{A}_c$ and $\mathbf{B}_c$ are defined as

$$\mathbf{A}_c = \begin{bmatrix} \mathbf{0} & \mathbf{I} \\ -\mathbf{M}^{-1}\mathbf{K} & -\mathbf{M}^{-1}\mathbf{D} \end{bmatrix} \quad 10)$$

$$\mathbf{B}_c = \begin{bmatrix} \mathbf{0} \\ [\mathbf{M}^{-1}\mathbf{K}\,\mathbf{L}, \mathbf{M}^{-1}\mathbf{D}\,\mathbf{L}] \end{bmatrix} \quad 11)$$

$\boldsymbol{w}(t)$ is a model noise (uncertainty) vector with zero mean and covariance matrix $\mathbf{Q}$. Absolute acceleration at any discrete-time instant i can be related to the state and FIMs as

$$\boldsymbol{y}[i] = \mathbf{E}\,\boldsymbol{z}[i] + \mathbf{F}\,\boldsymbol{f}[i] + \boldsymbol{v}[i] \quad 12)$$

where

$$\mathbf{E} = \mathbf{V}\,[-\mathbf{M}^{-1}\mathbf{K} \quad -\mathbf{M}^{-1}\mathbf{D}] \tag{13}$$

$$\mathbf{F} = \mathbf{V}\,[\mathbf{M}^{-1}\mathbf{K}\,\mathbf{L} \quad \mathbf{M}^{-1}\mathbf{D}\,\mathbf{L}] \tag{14}$$

in which $\mathbf{V}$ is an $l \times n$ matrix containing 1s and 0s to show which DOFs are measured. $\boldsymbol{v}[i]$ is a measurement noise vector assumed to be Gaussian zero-mean white with covariance matrix $\mathbf{R}$. $\boldsymbol{v}[i]$ represents difference between exact prediction, $\boldsymbol{h}[i] = \mathbf{E}\,\boldsymbol{z}[i] + \mathbf{F}\,\boldsymbol{f}[i]$ and real-life measurement $\boldsymbol{y}[i]$, i.e., $\boldsymbol{v}[i] = \boldsymbol{y}[i] - \boldsymbol{h}[i]$. According to the assumptions considered for this measurement noise, its Probability Distribution Function (PDF) can be expressed as

$$P(v) = \frac{1}{(2\pi)^{l/2}|\mathbf{R}|^{0.5}}\, e^{-\frac{1}{2}\boldsymbol{v}^T\mathbf{R}^{-1}\boldsymbol{v}} \tag{15}$$

where $|.|$ denotes determinant. Let's put all of the system's uncertain parameters (superstructure and IF parameters) into a vector $\boldsymbol{\theta} = [\theta_1 \quad \cdots \quad \theta_{n_\theta}]^T$. The unknown FIMs ($\boldsymbol{f}$) and system's parameters ($\boldsymbol{\theta}$) can be identified by maximization of joint PDF of $\boldsymbol{f}$ and $\boldsymbol{\theta}$ given measured responses. According to the Bayes' rule (Bayes, 1763), this a posteriori PDF can be expressed as

$$P(\boldsymbol{\theta}, \boldsymbol{f}|\boldsymbol{y}) = c\, P(\boldsymbol{y}|\boldsymbol{\theta}, \boldsymbol{f})\, P(\boldsymbol{\theta}, \boldsymbol{f}) \tag{16}$$

where $P(\boldsymbol{y}|\boldsymbol{\theta}, \boldsymbol{f})$ is the likelihood function, $P(\boldsymbol{\theta}, \boldsymbol{f})$ is the joint a priori PDF, and c is a constant. Assuming independences between $\boldsymbol{\theta}$ and $\boldsymbol{f}$ along with uniform PDFs for them (no initial information), maximization of $P(\boldsymbol{\theta}, \boldsymbol{f}|\boldsymbol{y})$ reduces to the maximization of likelihood function $P(\boldsymbol{y}|\boldsymbol{\theta}, \boldsymbol{f})$ (Ebrahimian, et al., 2015). This PDF at time instant $k+1$ can be calculated as

$$P(\boldsymbol{y}[1\!:\!k+1]|\boldsymbol{\theta}[k+1], \boldsymbol{f}[1\!:\!k+1]) = \prod_{i=1}^{k+1} P(\boldsymbol{v}[i]) \tag{17}$$

which can be rewritten as

$$P(\boldsymbol{y}[1\!:\!k+1]|\boldsymbol{\theta}[k+1], \boldsymbol{f}[1\!:\!k+1]) = \prod_{i=1}^{k+1} \frac{1}{(2\pi)^{l/2}|\boldsymbol{R}|^{0.5}}\, e^{-\frac{1}{2}\boldsymbol{v}[i]^T\boldsymbol{R}^{-1}\boldsymbol{v}[i]} \tag{18}$$

To maximize equation above, it is more convenient to minimize its negative natural logarithm—i.e., the following objective function:

$$J[k+1] = 1.83\,\frac{l(k+1)}{2} + \frac{1}{2}\sum_{i=1}^{k+1}|\mathbf{R}| + \frac{1}{2}\sum_{i=1}^{k+1}\boldsymbol{v}[i]^T\mathbf{R}^{-1}\boldsymbol{v}[i] \tag{19}$$

Two first terms on the right-hand side do not play a role in the objective function, because they are not updated. Thus, the objective function can be simplified as

$$J[k+1] = \sum_{i=1}^{k+1}\boldsymbol{v}[i]^T\mathbf{R}^{-1}\boldsymbol{v}[i] \tag{20}$$

As $\boldsymbol{h}[i]$ is a nonlinear function of $\boldsymbol{\theta}$, it should be linearized through Taylor's expansion so that the objective function becomes a quadratic function of $\boldsymbol{\theta}$ and $\boldsymbol{f}$. To do so, we can approximate $\boldsymbol{h}[i]$ as

$$\boldsymbol{h}[i] \approx \widehat{\boldsymbol{h}}[i] + \mathbf{H}_{\boldsymbol{\theta}}[i]\big(\boldsymbol{\theta}[i] - \widehat{\boldsymbol{\theta}}[i-1]\big) + \mathbf{H}_{\boldsymbol{f}}[i]\big(\boldsymbol{f}[i] - \widehat{\boldsymbol{f}}[i-1]\big) \tag{21}$$

where

$$\widehat{\boldsymbol{h}}[i] = \boldsymbol{h}\left[\hat{\boldsymbol{z}}[i|i-1], \widehat{\boldsymbol{\theta}}[i-1], \hat{\boldsymbol{f}}[i-1]\right] \tag{22}$$

$$\mathbf{H}_{\boldsymbol{f}}[i] = \left.\frac{\partial \boldsymbol{h}[i]}{\partial \boldsymbol{f}[i]}\right|_{\boldsymbol{z}[i]=\hat{\boldsymbol{z}}[i|i-1], \boldsymbol{\theta}[i]=\widehat{\boldsymbol{\theta}}[i-1], \boldsymbol{f}[i]=\hat{\boldsymbol{f}}[i-1]} \tag{23}$$

and $\mathbf{H}_{\boldsymbol{\theta}}[i] = \bar{\mathbf{H}}_{\boldsymbol{\theta}}[i] + \mathbf{H}_{\boldsymbol{z}}[i]\mathbf{Z}_{\boldsymbol{\theta}}[i]$ in which

$$\bar{\mathbf{H}}_{\boldsymbol{\theta}}[\boldsymbol{i}] = \left.\frac{\boldsymbol{\partial h}[\boldsymbol{i}]}{\boldsymbol{\partial \theta}[\boldsymbol{i}]}\right|_{\boldsymbol{z}[\boldsymbol{i}]=\hat{\boldsymbol{z}}[\boldsymbol{i}|\boldsymbol{i-1}], \boldsymbol{\theta}[\boldsymbol{i}]=\widehat{\boldsymbol{\theta}}[\boldsymbol{i-1}], \boldsymbol{f}[\boldsymbol{i}]=\hat{\boldsymbol{f}}[\boldsymbol{i-1}]} \tag{24}$$

$$\mathbf{H}_{\boldsymbol{z}}[i] = \left.\frac{\boldsymbol{\partial h}[i]}{\boldsymbol{\partial z}[i]}\right|_{\boldsymbol{z}[i]=\hat{\boldsymbol{z}}[i|i-1], \boldsymbol{\theta}[i]=\widehat{\boldsymbol{\theta}}[i-1], \boldsymbol{f}[i]=\hat{\boldsymbol{f}}[i-1]} \tag{25}$$

$$\mathbf{Z}_{\boldsymbol{\theta}}[i] = \left.\frac{\boldsymbol{\partial z}[i]}{\boldsymbol{\partial \theta}[i]}\right|_{\boldsymbol{\theta}[i]=\widehat{\boldsymbol{\theta}}[i-1]} \tag{26}$$

In the equations above, $\widehat{\boldsymbol{\theta}}[i-1]$ and $\hat{\boldsymbol{f}}[i-1]$ are, respectively, the estimation of $\boldsymbol{\theta}[i]$ and $\boldsymbol{f}[i]$ at the previous step, and $\hat{\boldsymbol{z}}[i|i-1]$ is an *a priori* estimation of state, which can be obtained by using these estimates through the state equation. That is

$$\hat{\boldsymbol{z}}[i|i-1] = \hat{\boldsymbol{z}}[i-1] + \mathbf{A}_c \Delta t\, \hat{\boldsymbol{z}}[i-1] + \mathbf{B}_c \Delta t\, \hat{\boldsymbol{f}}[i-1] \tag{27}$$

where Δt is the sampling time. $\mathbf{Z}_{\boldsymbol{\theta}}[i]$ is the sensitivity matrix of the state vector with respect to the system's parameters, and can be obtained by differentiating both sides of Eq. (27) with respect to $\boldsymbol{\theta}$ as

$$\mathbf{Z}_{\boldsymbol{\theta}}[i] = \mathbf{Z}_{\boldsymbol{\theta}}[i-1] + \Delta t\left\{\frac{\partial \mathbf{A}_c}{\partial \boldsymbol{\theta}[i]}\hat{\boldsymbol{z}}[i-1] + \mathbf{A}_c\, \mathbf{Z}_{\boldsymbol{\theta}}[i-1] + \frac{\mathbf{B}_c}{\partial \boldsymbol{\theta}[i]}\, \hat{\boldsymbol{f}}[i-1]\right\} \tag{28}$$

By substituting the approximation of $\boldsymbol{h}[i]$ into the objective function, we have

$$J[k+1] = \sum_{i=1}^{k+1}\big(\bar{\boldsymbol{y}}[i] - \mathbf{H}_{\boldsymbol{\theta}}[i]\boldsymbol{\theta}[i] - \mathbf{H}_{\boldsymbol{f}}[i]\boldsymbol{f}[i]\big)^T \boldsymbol{R}^{-1}\big(\bar{\boldsymbol{y}}[i] - \mathbf{H}_{\boldsymbol{\theta}}[i]\boldsymbol{\theta}[i] - \mathbf{H}_{\boldsymbol{f}}[i]\boldsymbol{f}[i]\big) \tag{29}$$

where

$$\bar{\boldsymbol{y}}[i] = \boldsymbol{y}[i] - \widehat{\boldsymbol{h}}[i] + \mathbf{H}_{\boldsymbol{\theta}}[i]\widehat{\boldsymbol{\theta}}[i-1] + \mathbf{H}_{\boldsymbol{f}}[i]\hat{\boldsymbol{f}}[i-1] \tag{30}$$

Huang et al. (2010) showed that the objective function of Eq. (29) can be minimized through following recursive solution

$$\hat{\boldsymbol{f}}[k+1] = \mathbf{S}[k+1]\mathbf{H}_{\boldsymbol{f}}[k+1]^T\mathbf{R}^{-1}(\boldsymbol{I} - \mathbf{H}_{\boldsymbol{\theta}}[k+1]\mathbf{G}_{\boldsymbol{\theta}}[k+1])(\boldsymbol{y}[k+1] - \hat{\boldsymbol{h}}[k+1] + \mathbf{H}_{\boldsymbol{f}}[k+1]\boldsymbol{f}[k]) \quad 31)$$

$$\hat{\boldsymbol{\theta}}[k+1] = \hat{\boldsymbol{\theta}}[k] + \mathbf{G}_{\boldsymbol{\theta}}[k+1]\{\boldsymbol{y}[k+1] - \mathbf{H}_{\boldsymbol{f}}[k+1](\hat{\boldsymbol{f}}[k+1] - \boldsymbol{f}[k])\} \quad 32)$$

where $\mathbf{G}_{\boldsymbol{\theta}}[k+1]$ is the Kalman Gain Matrix (Kalman, 1960) and is calculated as

$$\mathbf{G}_{\boldsymbol{\theta}}[k+1] = \mathbf{P}_{\boldsymbol{\theta}}[k]\mathbf{H}_{\boldsymbol{\theta}}[k+1]^T(\mathbf{R} + \mathbf{H}_{\boldsymbol{\theta}}[k+1]\mathbf{P}_{\boldsymbol{\theta}}[k]\mathbf{H}_{\boldsymbol{\theta}}[k+1]^T)^{-1} \quad 33)$$

in which $\mathbf{P}_{\boldsymbol{\theta}}[k]$ is the covariance matrix of the estimation error of $\boldsymbol{\theta}$, and is calculated as

$$\mathbf{P}_{\boldsymbol{\theta}}[k] = (\mathbf{I} + \mathbf{G}_{\boldsymbol{\theta}}[k]\mathbf{H}_{\boldsymbol{f}}[k]\mathbf{S}[k]\mathbf{H}_{\boldsymbol{f}}[k]^{\boldsymbol{T}}\mathbf{R}^{-1}\mathbf{H}_{\boldsymbol{\theta}}[k])(\mathbf{I} - \mathbf{G}_{\boldsymbol{\theta}}[k]\mathbf{H}_{\boldsymbol{\theta}}[k])\mathbf{P}_{\boldsymbol{\theta}}[k-1] \quad 34)$$

In the equations above, $\mathbf{S}[k+1]$ is also the covariance matrix of the estimation error of $\boldsymbol{f}$ and is obtained as

$$\mathbf{S}[k+1] = \{\mathbf{H}_{\boldsymbol{f}}[k+1]^T\mathbf{R}^{-1}(\mathbf{I} - \mathbf{H}_{\boldsymbol{\theta}}[k+1]\mathbf{G}_{\boldsymbol{\theta}}[k+1])\mathbf{H}_{\boldsymbol{f}}[k+1]^T\}^{-1}. \quad 35)$$

Once the system's parameters and the FIMs are updated at each iteration, the state of the system can be updated similarly. That is,

$$\hat{\boldsymbol{z}}[k+1|k+1] = \hat{\boldsymbol{z}}[k+1|k] + \mathbf{G}_{\boldsymbol{z}}[k+1]\{\boldsymbol{y}[k+1] - \hat{\boldsymbol{h}}[k+1]\} \quad 36)$$

with the Kalman Gain matrix being

$$\mathbf{G}_{\boldsymbol{z}}[k+1] = \mathbf{P}_{\boldsymbol{z}}[k+1|k]\mathbf{H}_{\boldsymbol{z}}[k+1]^{\boldsymbol{T}}(\mathbf{R} + \mathbf{H}_{\boldsymbol{z}}[k+1]\,\mathbf{P}_{\boldsymbol{z}}[k+1|k]\,\mathbf{H}_{\boldsymbol{z}}[k+1]^T)^{-1} \quad 37)$$

where $\mathbf{P}_{\boldsymbol{z}}[k+1|k]$ is an estimation of state error covariance matrix, obtained from the state equation as

$$\mathbf{P}_{\boldsymbol{z}}[k+1|k] = (\mathbf{I} + \mathbf{A}_c\Delta t\,)\mathbf{P}_{\boldsymbol{z}}[k](\mathbf{I} + \mathbf{A}_c\Delta t\,)^T + \mathbf{Q} \quad 38)$$

in which $\mathbf{P}_{\boldsymbol{z}}[k]$ is the last step's error covariance matrix calculated through

$$\mathbf{P}_{\boldsymbol{z}}[k] = (\mathbf{I} - \mathbf{G}_{\boldsymbol{z}}[k]\,\mathbf{H}_{\boldsymbol{z}}[k+1]\,)\mathbf{P}_{\boldsymbol{z}}[k|k-1]. \quad 39)$$

Remark 1: The size of the state vector will be very large, if it is directly applied on most of bridges under study in this project. However, as the method works under unknown excitation, it can be used through a sub-structuring approach. As an illustration, **Figure 7** displays the Antioch - San Joaquin River Bridge, which can be divided into four segments. The cut edges of each substructure are Neumann boundaries with unknown (to be estimated) excitations.

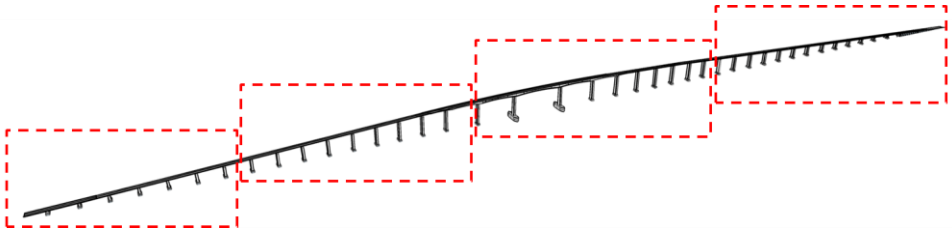

Figure 7. An example of proposed sub-structuring in CSMIP67771.

Remark 2: The proposed method works when the number of measurements is greater than the number of unknown FIMs. While this is almost always satisfied for the bridges under study, we rewrite $\hat{\boldsymbol{f}}[k+1]$ in state and observation equations—as well as other related equations versus acceleration—at the current time instant, and the displacement, velocity, and acceleration at the previous time step using Newmark's β-method (Chopra, 2001), as in

$$\hat{\boldsymbol{f}}[k+1] = \begin{bmatrix} \boldsymbol{x}_g[k+1]^T & \dot{\boldsymbol{x}}_g[k+1]^T \end{bmatrix}^T = \begin{bmatrix} \mathbf{T}_1 \hat{\bar{\boldsymbol{f}}}[k] + \\ \mathbf{T}_2 \hat{\bar{\boldsymbol{f}}}[k] + \end{bmatrix} + \begin{bmatrix} \beta \Delta t^2 \mathbf{I} \\ \gamma \Delta t \mathbf{I} \end{bmatrix} \ddot{\boldsymbol{x}}_g[k+1] \tag{40}$$

where $\hat{\bar{\boldsymbol{f}}}[k] = \left[x_{g_1}[k], \dot{x}_{g_1}[k], \ddot{x}_{g_1}[k], \cdots, x_{g_{n_g}}[k], \dot{x}_{g_{n_g}}[k], \ddot{x}_{g_{n_g}}[k] \right]$ and

$$\mathbf{T}_1 = \begin{bmatrix} \boldsymbol{\varphi}_1{}^T & & \\ & \ddots & \\ & & \boldsymbol{\varphi}_1{}^T \end{bmatrix}_{n_g \times 3n_g} \tag{41}$$

$$\mathbf{T}_2 = \begin{bmatrix} \boldsymbol{\varphi}_2{}^T & & \\ & \ddots & \\ & & \boldsymbol{\varphi}_2{}^T \end{bmatrix}_{n_g \times 3n_g} \tag{42}$$

in which $\boldsymbol{\varphi}_1 = [1 \quad \Delta t \quad (0.5-\beta)\Delta t^2]^T$ and $\boldsymbol{\varphi}_2 = [0 \quad 1 \quad (1-\gamma)\Delta t]^T$. Thus, at the $(k+1)^{\text{th}}$ iteration, $\hat{\bar{\boldsymbol{f}}}[k]$ is a known excitation and the unknown FIMs are collected in $\ddot{\boldsymbol{x}}_g[k+1]$. This, then, reduces the number of unknown excitations by a factor of two.

Remark 3: The proposed identification method is not limited to linear systems. As long as the soil, foundation, and structural nonlinearities can be incorporated into the system equations through parametric models, the proposed method can be used to identify those parameters that the said nonlinearities.

Remark 4: Having a reliable FE model of the bridge is an essential ingredient of the proposed identification method. For the present study, the geometry of these models for the studied bridges are based on SketchUp® models that are available through Google Earth®, which we then manually modify to obtain initial FE models. While the initial FE models are generally very accurate in geometry, they need to be improved by adding further details like constraints, connections, section properties, etc. The said details can be obtained through structural drawings. These modified FE are then employed along with the proposed identification method and data available in CESMD to identify the system parameters and FIMs. This process is schematically shown in **Figure 8**.

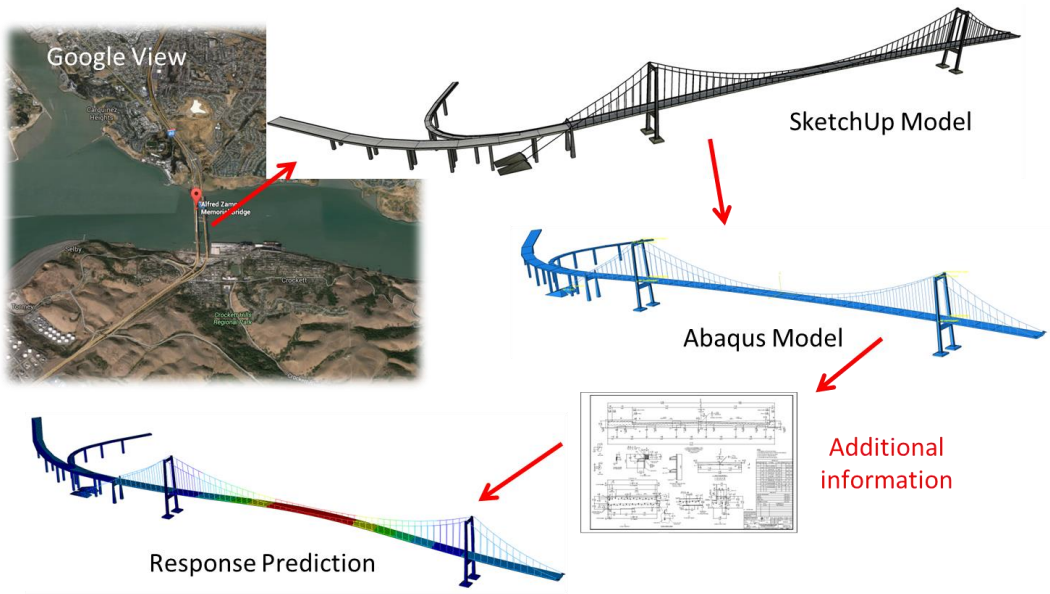

Figure 8. Initial FE modeling process.

Numerical Verification

To verify the proposed output-only identification method, we simulate the responses of a two-span bridge with continuous deck (**Figure 9**). It is assumed that mass of the foundation-bridge system is concentrated at 13 points, and there is no rotational mass moment of inertia. As such, stiffness and damping matrices can be statically condensed. Two horizontal ground motions recorded at the "Alhambra-1st & Woodward Station (CSMIP24030)" during 2001 West Hollywood earthquake are applied the remote ends of the soil-foundation springs at the two abutments (left- and right-ends) of the bridge as shown in **Figure 9**. Also, the abutment motion is multiplied by –1 and applied at the middle pier. These ground motions thus produce a combination of both independent and delayed input motions. Modulus of elasticity and moment of inertia of the deck beam are set at 1×10^9 and 0.05, respectively. Lumped masses, each with a value of 500, are placed at every 10 units of length. The stiffness of three springs are 12000, 12000, and 16000, respectively from left to right (all units are consistent). A Rayleigh damping with mass and stiffness factors of 0.2 and 0.002, respectively, is considered to create a classical damping matrix. Natural frequencies and modal damping ratios of this soil-foundation-bridge structure are listed in **Table 2**. As seen, the system is designed such that it is a fair representation of very long and flexible bridges that will be eventually studied in the present project.

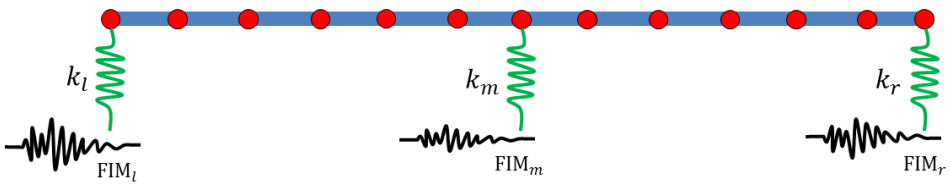

Figure 9. Synthetic bridge model with multiple support excitation.

Out of the 13 DOFs, only 5 channels (three foundations, left mid-span, and right mid-span) are used for identification. Stiffnesses of all tree springs, modulus of elasticity of the bridge, and the two damping coefficients are assumed as the system's unknown parameters (a total of 6 parameters) along with three FIM acceleration signals. **Figure 10** shows the convergence rate of estimation error for all of 6 parameters (as well as ±1 standard deviation). As seen, all errors converge to the zero. Standard deviation around the identified values quantifies how reliable these estimations are. For example, this figure indicates that while the identified damping parameters are very close to their exact values, the uncertainty in these identified values are relatively high compared to the identified spring stiffnesses and the elastic modulus.

The most important results of the identification process are the recovered FIMs. These signals are plotted together with their exact counterparts in **Figure 11**. As seen, the identified FIMs are very accurate. The standard deviation curves are not shown here, because they were very close to the identified signals. These results indicate that the proposed method will be a viable ingredient for the present project, and will produce accurate estimates of FIMs.

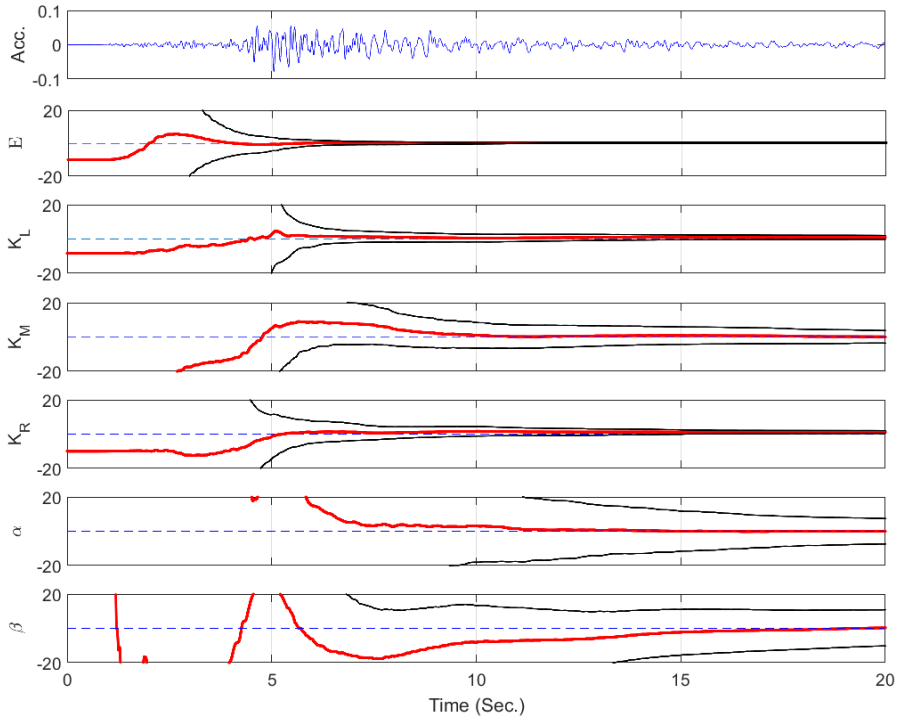

Figure 10. Error convergence rate.

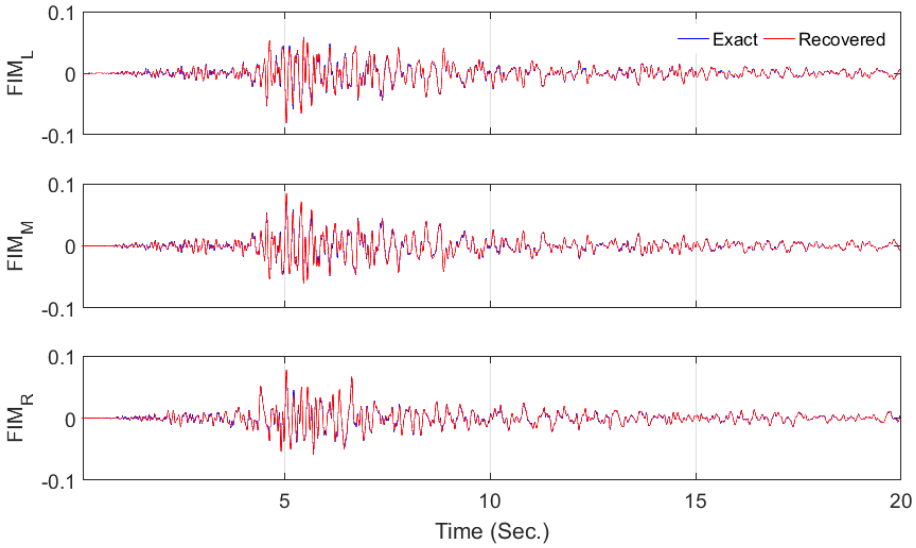

Figure 11. Comparison between exact and identified FIMs.

Table 2. Modal characteristics of the bridge model.

Mode No.	1	2	3	4	5	6	7	8	9	10	11	12	13
$f_n(Hz)$	0.30	0.36	0.65	0.84	1.29	1.97	2.93	4.07	5.40	6.85	8.35	9.69	10.67
$\xi_n(\%)$	5.43	4.59	2.87	2.42	2.04	2.05	2.39	2.95	3.69	4.54	5.43	6.25	6.85

Part II: Decomposition of FIMs to Site Response and Bedrock Motion

The identification of FIMs (e.g., through method described and verified in Part I above) enables a quantitative investigation of spatial variability in real-life ground motions. As already shown in **Figure 1**(right), these FIMs are filtered versions of a common bedrock motion[4] that pass through site response and kinematic interaction filters. Assuming that the kinematic interaction is the same for all piers, which is an acceptable assumption, we can extract the site-response Transfer Function at each pier through a blind channel identification method that will be described below. This new method is based on the assumption that a *common* bedrock motion passes through *different* sites. This means that the recovered bedrock motion is possibly altered by a kinematic interaction filter. While we shall only present a formulation for two sites (piers), the method can be easily extended to any number of sites (piers). In what follows, the ground surface motions represent those FIMs identified in Part I.

A soil deposit, e.g., **Figure 1**(left), can be assumed to be a Multi-Degree-Of-Freedom (MDOF) system with an infinite number of DOFs. Therefore, its dynamic response under rigid bedrock acceleration $\ddot{x}_b(t)$ can be expressed using modal superposition as (Glaser, 1996)

[4] Here, bedrock motion means motion at a location above which the response would be different at different locations. So, it may not be a physical bedrock, but rather a reference depth where the response is identical at different locations.

$$\ddot{x}_s(t) = \sum_{m=1}^{\infty} h_m(t) * \beta_m \ddot{x}_b(t) \tag{43}$$

where $*$ denotes a linear convolution; $\ddot{x}_s(t)$ is the absolute acceleration recorded on the ground surface; β_m is the modal contribution factor; and $h_m(t)$ is the IRF, which is given as (Ghahari, et al., 2013)

$$h_m(t) = \frac{1}{\omega_{d_m}} e^{-\xi_m \omega_{n_m} t}\left[\left(\omega_{d_m}^2 - \xi_m^2 \omega_{n_m}^2\right) sin\left(\omega_{d_m} t\right) + 2\xi_m \omega_{n_m} \omega_{d_m} cos(\omega_{d_m} t)\right] \tag{44}$$

Here ξ_m, ω_{n_m}, and $\omega_{d_m} = \omega_{n_m}\sqrt{1-\xi_m^2}$ denote the damping ratio, and the undamped and damped natural frequencies of the m-th mode, respectively. $h_m(t)$ is an Infinite Impulse Response (IIR) filter. The *Z*-Transform (Oppenheim, et al., 1989) of its discrete-time representation is

$$h_m(z) = \left[\frac{C_m + D_m z^{-1}}{1 - A_m z^{-1} - B_m z^{-2}}\right] \tag{45}$$

where

$$A_m = 2e^{-\xi_m \omega_{n_m} \Delta t}\, cos\left(\omega_{d_m} \Delta t\right), B_m = -e^{-2\xi_m \omega_{n_m} \Delta t},\ C_m = 2\xi_m \omega_{n_m} \Delta t,$$

$$D_m = \omega_{n_m}\, \Delta t\, e^{-\xi_m \omega_{n_m} \Delta t}\left[\frac{\omega_{n_m}}{\omega_{d_m}}\left(1 - 2\xi_m{}^2\right) sin\left(\omega_{d_m} \Delta t\right) - 2\xi_m cos(\omega_{d_m} \Delta t)\right]. \tag{46}$$

The Z-Transform helps to express the IRF in terms of the so-called poles (p_m and p_m^*), and zeros (z_m) as in

$$h_m(z) = C_m\,(z - z_m)/[(z - p_m)(z - p_m^*)] \tag{47}$$

where the superscript $*$ denotes a complex conjugate, and

$$z_m = -D_m/C_m, \qquad p_m, p_m^* = \frac{A_m \pm \sqrt{A_m{}^2 + 4B_m}}{2} \tag{48}$$

Indeed, the poles reflect the internal couplings within the system, while the zeros reflect the way the internal variables are coupled to the input and output signals (Åström, et al., 1984). Due to the frequency band of the bedrock motion, modal summation introduced in Eq. (43) is always finite; and the ground surface response signal can be well approximated by using a few fundamental modes, say n_m. So, Eq. (43) can be rewritten as

$$\ddot{x}_s(t) \cong \tilde{h}(t) * \ddot{x}_b(t) \tag{49}$$

where $\tilde{h}(t) = \sum_{m=1}^{n_m} \beta_m h_m(t)$. Based on the pole-zero representation mentioned above, we have

$$\tilde{h}(z) = \frac{\sum_{m=1}^{n_m}\left[\beta_m C_m (z - z_m)\prod_{l=1,l\neq m}^{n_m}(z-p_l)(z-p_l^*)\right]}{\prod_{m=1}^{n_m}(z-p_m)(z-p_m^*)} \quad 50)$$

The Proposed Algorithm

a. Decomposition

As shown in **Figure 1**(right), both sites (piers) are subject to an identical bedrock motion. So Eq. (49) can be written in discrete-time for both sites as

$$\ddot{x}_{s_1}[n] \cong \tilde{h}_1[n] * \ddot{x}_b[n] \quad 51)$$

$$\ddot{x}_{s_2}[n] \cong \tilde{h}_2[n] * \ddot{x}_b[n] \quad 52)$$

Thus, it is straightforward to show that the following cross-relation holds:

$$\ddot{x}_{s_1}[n] * \tilde{h}_2[n] = \ddot{x}_{s_2}[n] * \tilde{h}_1[n] \quad 53)$$

By applying a Z-Transform to both sites of the equation above, we can write

$$\ddot{x}_{s_1}[n]\,\tilde{h}_2(z) = \ddot{x}_{s_2}[n]\,\tilde{h}_1(z) \quad 54)$$

Based on Eq. (50), each $\tilde{h}_p(z)$ $(p = 1, 2)$ can be expressed as $N_p(z)/D_p(z)$ where $N_p(z)$ and $D_p(z)$ are polynomial functions of z. So, Eq. (54) can be restated as

$$\ddot{x}_{s_1}[n]\,N_2(z)D_1(z) = \ddot{x}_{s_2}[n]\,N_1(z)D_2(z), \quad 55)$$

which can be further restated in a simplified form as

$$\ddot{x}_{s_1}[n]\,g_1(z) = \ddot{x}_{s_2}[n]\,g_2(z) \quad 56)$$

where $g_1(z) = N_2(z)D_1(z)$ and $g_2(z) = N_1(z)D_2(z)$ are two Finite Impulse Response (FIR) filters. The order of polynomial g_1 (g_2) is equal to the sum of the orders of N_2 (or N_1) and D_1 (D_2), which is nominally $2n_{m,1} + 2n_{m,2} - 1$.

From the definition of the Z-Transform, Eq. (56) can be written by the discrete-time samples of $\ddot{x}_s[n]$ and the coefficients of polynomials $g(z)$—i.e., $g_p(z) = g_p[0] + g_p[1]z^{-1} + \cdots + g_p[1]z^{-(L-1)}$ —as follows

$$[\mathbf{X}_1 \quad -\mathbf{X}_2]\begin{bmatrix}\underline{\boldsymbol{g}}_1\\ \underline{\boldsymbol{g}}_2\end{bmatrix} = \mathbf{0} \quad 57)$$

where $\underline{\boldsymbol{g}}_p = [g_p[0] \quad g_p[1] \quad \cdots \quad g_p[L-1]]^T$ (for $p = 1,$ and 2) and

$$\mathbf{X}_p = \begin{bmatrix} \ddot{x}_{s_p}[L-1] & \ddot{x}_{s_p}[L-2] & \cdots & \ddot{x}_{s_p}[0] \\ \ddot{x}_{s_p}[L] & \ddot{x}_{s_p}[L-1] & \cdots & \ddot{x}_{s_p}[1] \\ \vdots & \vdots & \ddots & \vdots \\ \ddot{x}_{s_p}[N] & \ddot{x}_{s_p}[N-1] & \cdots & \ddot{x}_{s_p}[N-L+1] \end{bmatrix}_{(N-L+1)\times L} \quad \text{for} \quad p = 1, 2 \qquad 58)$$

where $L = 2n_{m,1} + 2n_{m,2}$, and N denotes the number of recorded samples. Eq. (57) is a classical equation in the field of Single-Input-Multiple-Output (SIMO) blind channel identification (Xu, et al., 1995; Moulines, et al., 1995; Gürelli & Nikias, 1995). It is a system of $(N - L + 1)$ linear homogenous equations with $2L$ unknowns, which can have a unique solution (up to an arbitrary scaling factor), provided that the number of sample points are adequate $N \geq 3L - 1$ (which is always satisfied in our cases). Indeed, the matrix $[\mathbf{X}_1 \quad -\mathbf{X}_2]$ is rank deficient by 1, and the solution, $[\underline{\boldsymbol{g}}_1 \quad \underline{\boldsymbol{g}}_2]^T$, would be the one-dimensional null space of the matrix, which can be identified as its *right singular vector* corresponding to the zero singular value.

In real-life, due to the presence of noise and modeling errors, Eq. (57) is only approximately valid. In other words, the matrix $[\mathbf{X}_1 \quad -\mathbf{X}_2]$ is full-rank, because the theoretical zero singular value is lost within the noise-corrupted singular values. So, there is no null subspace in the space created by the columns. Therefore, $[\underline{\boldsymbol{g}}_1 \quad \underline{\boldsymbol{g}}_2]^T$ will be the right singular vector corresponding to the *smallest* singular value.

Once $\underline{\boldsymbol{g}}_1$ and $\underline{\boldsymbol{g}}_2$ are identified, the site's Transfer Functions can be easily reconstructed, provided that we can accurately decompose $\underline{\boldsymbol{g}}_1$ ($\underline{\boldsymbol{g}}_2$) to $N_1(z)$ ($N_2(z)$) and $D_1(z)$ ($D_2(z)$). In the following section, we describe an algorithm for the said decomposition.

b. Zero-Pole Pairing, Order Estimation, and Identification of Modal Contribution Factors

Let's assume that we have overestimated the number of modes at each site as $\tilde{n}_{m,1} = n_{m,1} + \bar{n}_{m,1}$ and $\tilde{n}_{m,2} = n_{m,2} + \bar{n}_{m,2}$. Therefore, L is overestimated as $\tilde{L} = L + \bar{L}$ where $\bar{L} = 2(\bar{n}_{m,1} + \bar{n}_{m,2})$. In other words, polynomials $g_1(z)$ and $g_2(z)$ obtained via Eq. (57) have $\bar{L}$ extraneous zeros. But, to satisfy Eq. (56), these $\bar{L}$ extraneous zeros must appear at the same locations[5] for both $g_1(z)$ and $g_2(z)$. Thus, in the absence of noise, $\bar{L}$ can be identified as the dimension of the null space of $[\mathbf{X}_1 \quad -\mathbf{X}_2]$ minus one.

Measurement noise is inevitable, especially in the FIMs recovered from real-life data. As such, the number of zero singular values of $[\mathbf{X}_1 \quad -\mathbf{X}_2]$ would not be helpful to determine the number of extraneous zeros (i.e., $\bar{L}$) or their locations. Here, we make use of stability diagrams (Bodeux & Golinval, 2001) to circumvent this problem. We solve Eq. (57) for a range of $\tilde{L}$ (in 2 incremental steps) and repeat the following steps for each case:

1. Calculate the natural frequencies and damping ratios via equations below for all recovered roots without regarding to these roots being poles, zeros, or extraneous zeros (this information is yet known).

$$\omega_{n_m} = \left|\frac{ln\, p_m}{\Delta t}\right| \qquad 59)$$

[5] We assume here that the two sites have dissimilar poles and zeros.

$$\xi_m = -Re\left\{\frac{ln\, p_m}{\Delta t}\right\}/\omega_{n_m} \tag{60}$$

2. Exclude those roots that predict unusual damping ratios—i.e., negative or higher than %100.
3. Find the closest natural frequency from the previous step for each natural frequency, and calculate the following frequency and damping ratio errors:

$$E(\omega_m) = \frac{\left|\omega_{m,\tilde{L}_i} - \omega_{m,\tilde{L}_{i-1}}\right|}{\omega_{m,\tilde{L}_{i-1}}}, \qquad E(\xi_m) = \frac{\left|\xi_{m,\tilde{L}_i} - \xi_{m,\tilde{L}_{i-1}}\right|}{\xi_{m,\tilde{L}_{i-1}}} \tag{61}$$

4. Accept those modes having frequency and damping errors that are less than pre-specified thresholds as stable roots of $D_1(z)$ and $D_2(z)$.

By plotting the stable roots versus frequency, the actual modes will be revealed, as they will appear as vertical lines on these (stability) plots. So, not only $n_{m,1}$ and $n_{m,2}$ are identified as being the number of stable vertical lines on stability diagram, but also the poles can be picked. Finally, the modal contribution factors can be estimated through the method described (Ghahari, et al., 2016).

c. Bedrock Motion Estimation

Having fully identified $\tilde{h}(z)$ of both sites, the bedrock acceleration, $\ddot{x}_b[n]$, can now be recovered from any of the recorded ground surface signals by inverting $\tilde{h}(z)$, provided that such inversion produces a stable system. Nevertheless, there is no guarantee that our systems will have zeros inside the unit circle, so we have to design Finite Impulse Response (FIR) de-convolution filters $W_1(z)$ and $W_2(z)$ such that

$$\ddot{x}_b[n] = W_1(z)\, \ddot{x}_{s_1}[n] + W_2(z)\, \ddot{x}_{s_2}[n]. \tag{62}$$

In what follows, the process to calculate these FIR deconvolution filters is described. Assuming that the numerator polynomials $N_1(z)$ and $N_2(z)$ have no common zeros, we can find polynomials $V_1(z)$ and $V_2(z)$ for which the following Diophantine polynomial equation is valid

$$N_1(z)\, V_1(z) + N_2(z)\, V_2(z) = 1. \tag{63}$$

The solution of the Diophantine polynomial equation above—i.e., determination of the coefficients of the polynomials $V_1(z)$ and $V_2(z)$—is achieved through the inversion of the following linear system

$$\begin{bmatrix} \mathbf{M}_1 & \mathbf{M}_2 \\ \mathbf{0}_{2(n_1-n_2)\times n_2} & \end{bmatrix} \begin{bmatrix} \underline{\boldsymbol{V}}_1 \\ \underline{\boldsymbol{V}}_2 \end{bmatrix} = \begin{bmatrix} \mathbf{1} \\ \mathbf{0}_{(n_1+n_2)\times 1} \end{bmatrix} \tag{64}$$

where $\underline{\boldsymbol{V}}_1 = [\, V_1[0] \quad V_1[1] \quad \cdots \quad V_1[n_1-1]]^T$, $\underline{\boldsymbol{V}}_2 = [\, V_2[0] \quad V_2[1] \quad \cdots \quad V_1[n_2-1]]^T$, and $\mathbf{M}_1$ and $\mathbf{M}_2$ are the Sylvester matrices defined as below

$$\mathbf{M}_1 = \begin{bmatrix} N_1[0] & & & 0 \\ \vdots & N_1[0] & & \\ N_1[n_1-1] & \vdots & \ddots & \\ & N_1[n_1-1] & & N_1[0] \\ & & \ddots & \vdots \\ 0 & & & N_1[n_1-1] \end{bmatrix}_{(2n_1-1)\times n_1} \quad (65)$$

$$\mathbf{M}_2 = \begin{bmatrix} N_2[0] & & & 0 \\ \vdots & N_2[0] & & \\ N_2[n_2-1] & \vdots & \ddots & \\ & N_2[n_2-1] & & N_2[0] \\ & & \ddots & \vdots \\ 0 & & & N_2[n_2-1] \end{bmatrix}_{(2n_2-1)\times n_2} \quad (66)$$

In the equations above, $n_1 = 2n_{m,1} + 1$ and $n_2 = 2n_{m,2} + 1$ ($n_1 \geq n_2$) denote the number of coefficients of the polynomial $N_1(z)$ and $N_2(z)$, respectively. Now, by multiplying both sides of Eq. (63) with $\ddot{x}_b[n]$, we get

$$\ddot{x}_b[n]\, N_1(z)\, V_1(z) + \ddot{x}_b[n]\, N_2(z)\, V_2(z) = \ddot{x}_b[n] \quad (67)$$

and by replacing $\ddot{x}_b[n]\, N_1(z)$ and $\ddot{x}_b[n]\, N_2(z)$ by $\ddot{x}_{s_1}[n]\, D_1(z)$ and $\ddot{x}_{s_2}[n]\, D_2(z)$, respectively, we have

$$\ddot{x}_{s_1}[n]\, D_1(z)\, V_1(z) + \ddot{x}_{s_2}[n]\, D_2(z)\, V_2(z) = \ddot{x}_b[n] \quad (68)$$

By comparing Eqs. (62) and (68) it can be concluded that the FIR deconvolution filters $W_1(z)$ and $W_2(z)$ are

$$W_1(z) = D_1(z)\, V_1(z) \quad (69)$$

$$W_2(z) = D_2(z)\, V_2(z) \quad (70)$$

It is expedient to note here that the recovered bedrock motion is identified to within a scaling ambiguity. Due to this scaling ambiguity, it is possible to extract two bedrock motions by either $W_1(z)\, \ddot{x}_{s_1}[n]$ or $W_2(z)\, \ddot{x}_{s_2}[n]$.

Numerical Verification

To verify the proposed method, we modeled two sites with different properties as shown in **Table 3**. We considered a cubic variation of shear wave velocity with respect to depth in one site to keep the simulation as realistic/complex as possible. Natural frequencies and modal contribution factors of modes below 10 Hz are shown in **Table 4**. We limited our simulation below 10 Hz, which is typically the frequency range of interest in earthquake engineering applications. **Figure 12** displays the exact Transfer Functions of two sites within the frequency range of interest, which exhibit four and three modes that are contributing to the responses of Sites 1 and 2, respectively. As seen in this figure, the modes of both sites are very close to each

other. This brings more realism to the simulation, because it is reasonable to observe close modes for two neighboring sites.

Ground surface responses are generated by assuming vertically propagating shear waves from rigid bedrock. To make the problem as realistic as possible, ground accelerations recorded by the Corona I-15/Hwy-91 geotechnical array (CSMIP Station 13186) during the 2008 Chino Hills Earthquake at a depth of 42 meters are used as the bedrock motion. Based on the P-S logging test data available at the Center for Engineering Strong Motion Data (CESMD) database, the recorded signal at this level mimics accurately a rock motion. **Figure 13** displays the acceleration time-history of the selected bedrock excitation. In addition to the noise-free simulated data, we also analyzed a noisy case by adding Gaussian distributed white noise with Root-Mean-Square of ~10% of the generated ground surface signals (equivalent SNR = 20).

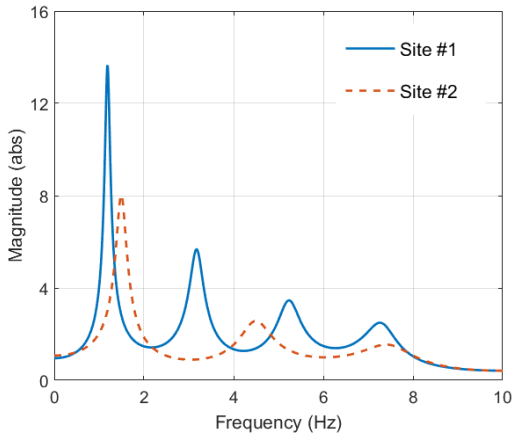

Figure 12. Exact Transfer Functions of two sites under study.

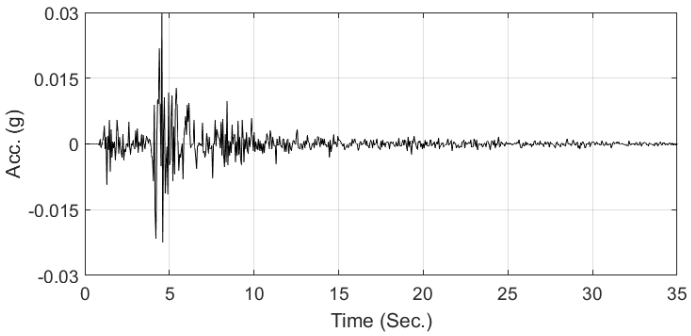

Figure 13. Bedrock acceleration (last accessed on 2/17/2016 at www.strongmotioncenter.org).

Table 3. Soil profiles at two sites.

Site	ρ (kg/m^3)	H (m)	Surface V_s (m/s)	Bottom V_s (m/s)	V_s Variation	ξ (%)*
1	2000	50	150	300	Cubic	5.00
2	2300	50	300	300	Constant	8.00

* The proposed method works for general case of having different modal damping ratios, but it is believed soil's damping is constant for all modes (Park & Hashash, 2004).

Table 4. Natural frequencies (Hz) and modal contribution factors at two sites.

	Site	1	2	3	4
Natural Frequency (Hz)	1	1.19	3.18	5.24	7.30
	2	1.50	4.50	7.50	---
Contribution Factor	1	1.37	−0.57	0.35	−0.26
	2	1.27	−0.42	0.25	---

We first assume that we know the exact number of contributing modes at each site. So, Eq. (57) is solved in one step and the roots of the polynomials $g_1(z)$ and $g_2(z)$ are identified.

Figure 14 shows the comparison between the actual poles and zeros of the two sites and the identified values. As the type of the roots (poles or zero) is not yet known, the identified roots are shown by circles. This figure shows that for the noise-free case, the identified roots match the actual roots perfectly. In the presence of noise, the locations of the poles are still accurate, but the zeros are identified with significant errors. Before employing stability diagram to classify roots as zeros and poles, it is useful to see what we would get if we consider all of the recovered roots as poles; and this comparison should clarify the utility of the algorithm described in §b above.

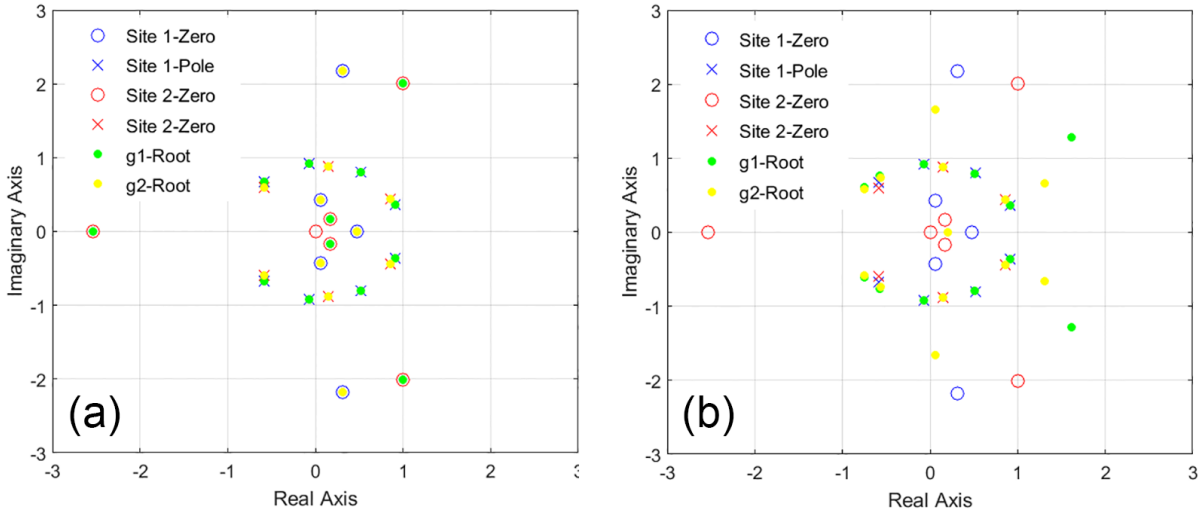

Figure 14. Comparison of the poles and zeros of two systems and roots of $g_1(z)$ and $g_2(z)$ that are recovered through Eq. (57) for (a) noise-free and (b) noisy cases.

Assuming that all of the recovered roots are poles, we can calculate the natural frequencies and damping ratios using Eqs. (59) and (60), respectively. These values are reported in **Table 5** and **Table 6** for the noise-free and the noisy cases, respectively. As seen, the zeros labeled as poles result in unusual damping ratios (see columns 5, 6, 7, 8, and 13 for Site #1 and columns 3, 4, 7, 8 9, 10, and 13 for the Site #2 in **Table 5**). While unusual damping values are observed for most of the spurious poles for the noisy case, there are a few cases that have reasonable damping ratios, which renders the pole picking step inevitable.

Table 5. Candidates of natural frequencies and damping ratios (noise-free case).

	1	2	3	4	5	6	7	8	9	10	11	12	13
Identified Modal Parameters from $g_1(z)$													
$f_n(Hz)$	1.19	1.19	3.18	3.18	4.36	4.36	5.13	5.13	5.24	5.24	7.30	7.30	10.43
$\xi_n(\%)$	5	5	5	5	−58.8	−58.8	87.4	87.4	5	5	5	5	−28.4
Identified Modal Parameters from $g_2(z)$													
$f_n(Hz)$	1.50	1.50	2.35	3.57	4.50	4.50	5.19	5.19	5.28	5.28	7.50	7.50	13.26
$\xi_n(\%)$	8	8	100	−100	8	8	−48.3	−48.3	50.7	50.7	8	8	−65.7

Table 6. Candidates of natural frequencies and damping ratios (noisy case).

	1	2	3	4	5	6	7	8	9	10	11	12	13
	Identified Modal Parameters from $g_1(z)$												
$f_n(Hz)$	1.19	1.19	3.13	3.13	3.18	3.18	5.26	5.26	7.08	7.08	7.81	7.81	7.92
$\xi_n(\%)$	5	5	−73.2	−73.2	5.5	5.5	5.2	5.2	2.0	2.0	1.4	1.4	−100
	Identified Modal Parameters from $g_2(z)$												
$f_n(Hz)$	1.50	1.50	1.91	1.91	4.50	4.50	5.02	5.14	5.14	7.07	7.07	7.90	7.90
$\xi_n(\%)$	8.3	8.3	−63.7	−63.7	7.5	7.5	100	−31.5	−31.5	3.3	3.3	2.1	2.1

In addition to the observations above, we assumed, up to now, that we know the exact number of modes of two sites, which is often not possible in real-life. Also, due to presence of noise, it is necessary to increase the number of roots of $g_1(z)$ and $g_2(z)$ and then to discard the extraneous roots. As such, we carry out the procedure described in §b. We solve Eq. (57) for a range of $\tilde{L}$ from 14 (exact for the noise free) up to 40.

Figure 15 displays all singular values of the matrix $[\mathbf{X}_1 \quad -\mathbf{X}_2]$ corresponding to each order value. Instead of $\tilde{L}$, we use $L^{-}+1$ for the X-axis, because the number of small singular values for each case must be theoretically equal to $L^{-}+1$. As seen from this figure, such relationship is observed for the noise-free case wherein the X-axis denotes the number of small singular values. Yet, a similar observation cannot be made for the noisy case. As such, we cannot determine the exact order of the problem by counting the number of small singular values. Instead, we take advantage of the stability diagram shown in **Figure 16**. In this figure, the roots that have rational/justifiable damping ratios (between zero and %100) are shown by cross marks. As seen, for the theoretical value of L=14, two close frequencies are identified for both sites for the last mode (See **Table 5** and **Table 6**) in the noisy case, and none of them are correct.

By applying the stability criteria $E(\omega_m) \leq \%1$ and $E(\xi_m) \leq \%15$[6], stable modes are detected, which are marked by red circles. As seen, four and three stable vertical lines are clearly detected for Sites #1 and #2, respectively, for both the noise-free and the noisy cases. Also, values of the natural frequencies and damping ratios of these 7 modes are easily obtained from the stable modes at the last $\tilde{L}$ value. These values are reported in **Table 7**. Also, using approach described in (Ghahari, et al., 2016), the modal contribution factors are identified. As seen, the natural frequencies, damping ratios, and modal contribution factors are highly accurate. To visualize the accuracy of the identified results, the exact and reconstructed transfer functions of the noisy case are shown in **Figure 17** (noise-free transfer functions are perfectly matched).

[6] It is well accepted that estimated damping ratios are highly unstable, so we allow much larger variation for damping compared to the natural frequency.

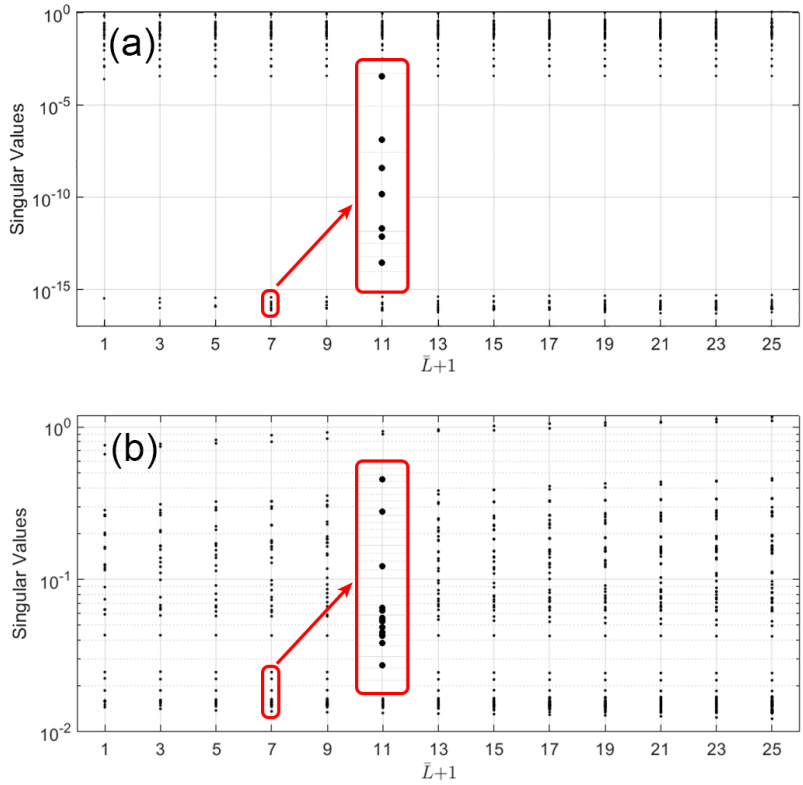

Figure 15. Distribution of singular values versus $\bar{L}+1$ for (a) noise free and (b) noisy cases.

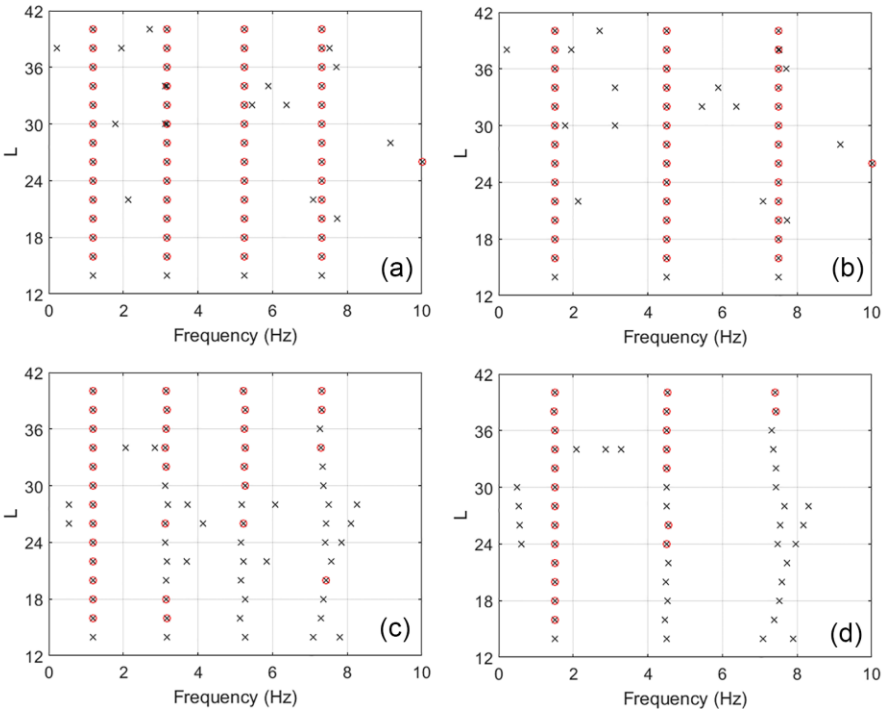

Figure 16. Stability diagrams for (a) Site #1, noise-free, (b) Site #2, noise-free, (c) Site #1, noisy, and (d) Site #2, noisy cases.

Table 7. Comparison between exact and identified modal properties through stability approach.

	Site #1									Site #2								
	$f_n(Hz)$			$\xi_n(\%)$			β_n			$f_n(Hz)$			$\xi_n(\%)$			β_n		
Mode No.	0*	1†	2‡	0	1	2	0	1	2	0	1	2	0	1	2	0	1	2
1	1.19	1.19	1.19	5	5	4.9	1.37	1.37	1.37	1.50	1.50	1.50	8	8	8.3	1.27	1.27	0.97
2	3.18	3.18	3.14	5	5	5.8	−0.57	−0.56	−0.52	4.50	4.50	4.53	8	8	7.4	−0.42	−0.41	−0.51
3	5.24	5.24	5.23	5	5	4.8	0.35	0.34	0.38	7.50	7.50	7.42	8	8	5.2	0.25	0.25	0.18
4	7.30	7.30	7.33	5	5	3.3	−0.26	−0.25	−0.19	---	---	---	---	---	---	---	---	---

* Exact, † Identified from noise-free data, ‡ Identified from noisy data

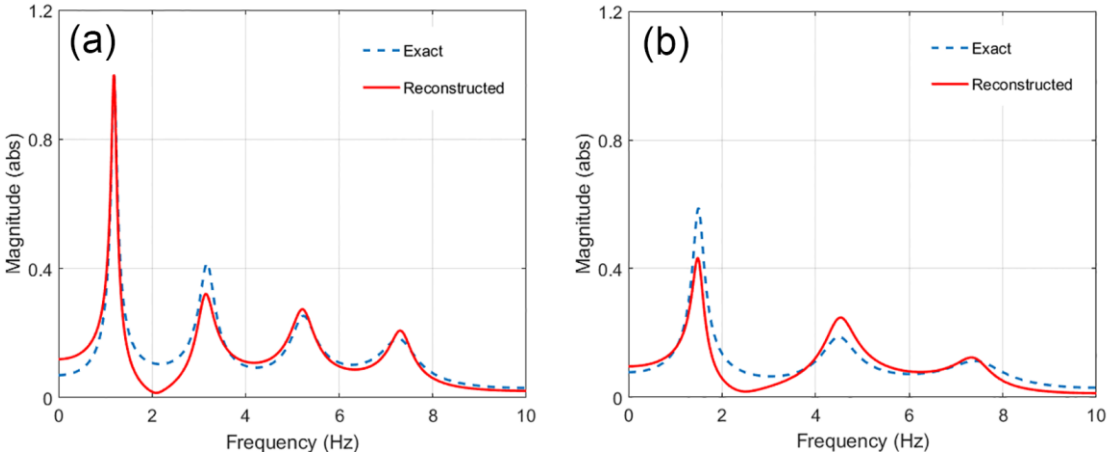

Figure 17. Comparison between the exact and the reconstructed Transfer Functions obtained from noisy data using the stability approach for (a) Site #1 and (b) Site #2.

Now, by having both sites' Transfer Functions identified using the stability diagram approach, we can recover the bedrock motion from recorded ground surface accelerations through approach proposed in §d. The recovered bedrock motion using the said approach is compared with the exact bedrock motion in **Figure 18** in the frequency domain. It is not surprising to see a near-perfect match for the noise-free case, because both the recorded signals and identified systems are exact. For the noisy cases, there are two sources of error observed between the exact and the identified results. First, as it was shown in **Figure 17**, the systems are not identified perfectly and thus we expect to see some errors, especially around 1Hz (see also **Figure 17**b). Second, the recorded signals are highly noisy, so the recovered bedrock motion is a noisy version of the actual bedrock motion. This source of error is mostly observed for high frequencies, where the system's Transfer Function has little amplification.

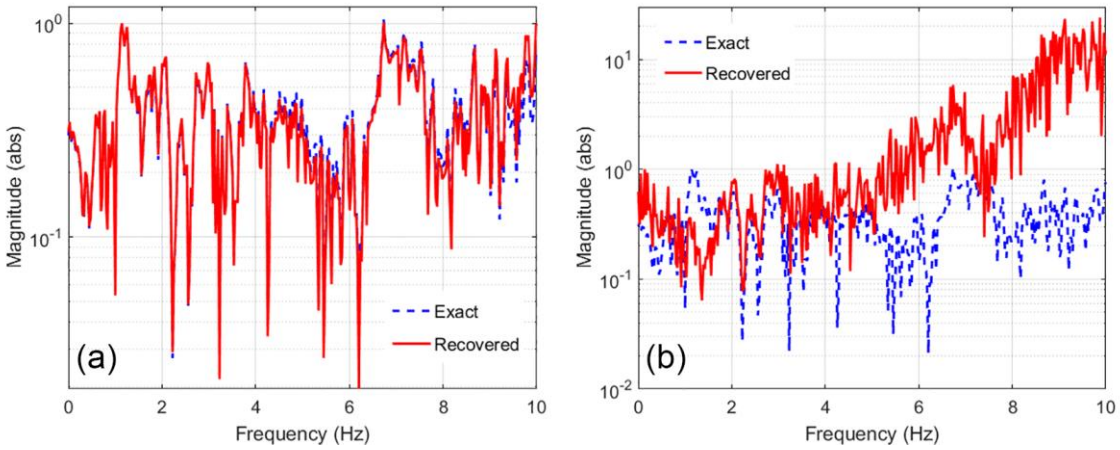

Figure 18. Comparison between Fourier spectrum of exact and recovered bedrock motion for (a) noise free and (b) noisy cases.

Conclusions

This study presented the theoretical basis for an ongoing CGS-funded project whose ultimate objective is to quantify the spatial variability in *bridge* Foundation Input Motions (FIMs) using data recorded during the 2014 South Napa Earthquake. This aspect comprised the development and verification of two distinct (and new) methods. The first of these was an output-only system identification method that yields time-history estimates of FIMs at all bridge piers from accelerations recorded on the bridge. The second was a blind channel identification method that enables the identification of local site effects at each pier provided that all FIMs are caused by a single excitation source and the kinematic interaction is similar at all piers. While these assumptions (especially the latter) can be relaxed, as needed, in future studies, the two methods will combine to produce quantified estimates of spatial variability in real-life ground motions. The accuracy of these two key methods was verified in the present study through synthetic, albeit realistic, datasets.

In addition to developing and verifying the two methods required to achieve the project's objectives, the present study allowed the determination of datasets from the 2014 event that are amenable to detailed analyses (short bridges, and bridges with missing data were excluded). It also provided preliminary evidence—simply by using signals recorded at the foundation levels of instrumented bridges—that there is indeed significant spatial variability in real-life ground motion. The results of the application of the proposed approach to the real-life data recorded during the 2014 event will be presented in SMIP17.

Acknowledgements

The work presented in this manuscript was funded, in part, by the California Geological Survey (Contract No. 1014-963) and by the California Department of Transportation (Grant No. 65A0450). Any opinions, findings, conclusions or recommendations expressed in this material are those of the authors and do not necessarily reflect the views of the sponsoring agencies.

References

Åström, K., Hagander, P. & Sternby, J., 1984. Zeros of sampled systems. *Automatica,* 20(1), 31-38.

Bayes, T., 1763. An essay towards solving a problem in the doctrine of chances. *Philosophical Transactions of the Royal Society of London,* 53(1), 370-418.

Bendat, J. & Piersol, A., 1980. Engineering applications of correlation and spectral analysis. New York: John Wiley.

Bodeux, J. & Golinval, J., 2001. Application of ARMAV models to the identification and damage detection of mechanical and civil engineering structures. *Smart Materials and Structures,* 10, 479-489.

Burdette, N., Elnashai, A., Lupoi, A. & Sextos, A., 2008. Effect of asynchronous earthquake motion on complex bridges. I: methodology and input motion. *J. of Bridge Eng.,* 13(2), 158-165.

Chopra, A., 2001. *Dynamics of Structures.* 2nd ed., Prentice-Hall, Englewood Cliffs, NJ.

Ebrahimian, H., Astroza, R. & Conte, J., 2015. Output-only identification of civil structures using nonlinear finite element model updating. San Diego, SPIE, pp. 1-9.

Ghahari, S., Abazarsa, F., Ghannad, M. & Taciroglu, E., 2013. Response-only modal identification of structures using strong motion data. *Earthquake Engineering and Structural Dynamics,* 42(8),1221-1242.

Ghahari, S. et al., 2016. Blind identification of site effects and bedrock motions from surface response signals. *Soil Dynamics and Earthquake Engineering,* (under review).

Glaser, S., 1996. Insight into liquefaction by system identification. *Geotechnique,* 46(4), 641-655.

Gürelli, M. & Nikias, C., 1995. EVAM: An eigenvector-based algorithm for multichannel blind deconvolution of input colored signals. *IEEE Trans. on Signal Processing,* 43(1), pp. 134-149.

Hao, H., Bolt, B. & Penzien, J., 1989. Effects of spatial variation of ground motions on large multiply-supported structures: Earthquake Engineering Research Center.

Huang, H., Yang, J. & Zhou, L., 2010. Adaptive quadratic sum-squares error with unknown inputs for damage identification of structures. *Struct. Control & Health Mon.,* 17(4), 404-426.

Kalman, R., 1960. A new approach to linear filtering and prediction problems. *Journal of basic Engineering,* 82(1), 35-45.

Kurata, M. et al., 2012. Internet-enabled wireless structural monitoring systems: development and permanent deployment at the new Carquinez suspension bridge. *Journal of Structural Engineering,* 139(10), 1688-1702.

Lupoi, A., Franchin, P., Pinto, P. & Monti, G., 2005. Seismic design of bridges accounting for spatial variability of ground motion. *Earthquake Engineering & Structural Dynamics,* 34(4-5), 327-348.

Moulines, E., Duhamel, P., Cardoso, J. & Mayrargue, S., 1995. Subspace methods for the blind identification of multichannel FIR filters. *IEEE Transactions on Signal Processing,* 43(2), 516-525.

Nazmy, A. & Abdel-Ghaffar, A., 1992. Effects of ground motion spatial variability on the response of cable-stayed bridges. *Earthquake Engineering & Structural Dynamics,* 21, 1-20.

Oppenheim, A., Schafer, R. & Buck, J., 1989. *Discrete-Time Signal Processing* (2nd ed.), Prentice-Hall, Englewood Cliffs, NJ.

Park, D. & Hashash, Y., 2004. Soil damping formulation in nonlinear time domain site response analysis. *Journal of Earthquake Engineering,* 8(02), 249-274.

Shakal, A., Haddadi, H. & Huang, M., 2014. Highlights of strong-motion data from the M6.0 South Napa earthquake of August 24, 2014, Calif. Geological Survey, pp. 111-130.

Xu, G., Liu, H., Tong, L. & Kailath, T., 1995. A least-squares approach to blind channel identification. *IEEE Transactions on Signal Processing,* 43(12), 2982-2993.

Zerva, A., Ang, A. & Wen, Y., 1988. Lifeline response to spatially variable ground motions. *Earthquake Engineering & Structural Dynamics,* 16(3), 361-379.

Zerva, A. & Zervas, V., 2002. Spatial variation of seismic ground motions: An overview. *Applied Mechanics Reviews,* 55(3), 271-297.